

## THE EQUATION OF STATE FROM OBSERVED MASSES AND RADII OF NEUTRON STARS

ANDREW W. STEINER<sup>1</sup>, JAMES M. LATTIMER<sup>2</sup>, AND EDWARD F. BROWN<sup>1</sup>

<sup>1</sup> Department of Physics & Astronomy, National Superconducting Cyclotron Laboratory, and the Joint Institute for Nuclear Astrophysics, Michigan State University, East Lansing, MI, USA; [steinera@pa.msu.edu](mailto:steinera@pa.msu.edu), [ebrown@pa.msu.edu](mailto:ebrown@pa.msu.edu)

<sup>2</sup> Department of Physics & Astronomy, Stony Brook University, Stony Brook, NY, USA; [lattimer@mail.astro.sunysb.edu](mailto:lattimer@mail.astro.sunysb.edu)

Received 2010 May 11; accepted 2010 August 4; published 2010 September 15

### ABSTRACT

We determine an empirical dense matter equation of state (EOS) from a heterogeneous data set of six neutron stars: three Type-I X-ray bursters with photospheric radius expansion, studied by Özel et al., and three transient low-mass X-ray binaries. We critically assess the mass and radius determinations from the X-ray burst sources and show explicitly how systematic uncertainties, such as the photospheric radius at touchdown, affect the most probable masses and radii. We introduce a parameterized EOS and use a Markov chain Monte Carlo algorithm within a Bayesian framework to determine nuclear parameters such as the incompressibility and the density dependence of the bulk symmetry energy. Using this framework we show, for the first time, that these parameters, predicted solely on the basis of astrophysical observations, all lie in ranges expected from nuclear systematics and laboratory experiments. We find significant constraints on the mass–radius relation for neutron stars, and hence on the pressure–density relation of dense matter. The predicted symmetry energy and the EOS near the saturation density are soft, resulting in relatively small neutron star radii around 11–12 km for  $M = 1.4 M_{\odot}$ . The predicted EOS stiffens at higher densities, however, and our preferred model for X-ray bursts suggests that the neutron star maximum mass is relatively large,  $1.9\text{--}2.2 M_{\odot}$ . Our results imply that several commonly used equations of state are inconsistent with observations.

**Key words:** dense matter – stars: neutron – X-rays: binaries – X-rays: bursts

*Online-only material:* color figures

### 1. INTRODUCTION

The masses and radii of neutron stars are determined by the pressure–energy density relation (equation of state; EOS hereafter) of cold dense matter using the familiar Tolman–Oppenheimer–Volkov (TOV; Tolman 1939; Oppenheimer & Volkoff 1939) relativistic stellar structure equations. Within tens of seconds after birth, the neutron star is cold (meaning temperature is much less than Fermi energy) and deleptonized (meaning it is in beta equilibrium with no trapped neutrinos); as a result, for a given EOS the mass and radius of the star depend only on the central density. Inversion of the structure equations, given simultaneous mass and radius measurements, can therefore constrain the pressure–density relation, although the quality of the constraints are very sensitive to the mass and radius measurement uncertainties.

A host of observable phenomena and experimental information is becoming available (for a recent review, see Lattimer & Prakash 2007): on the observational side, pulsar timing, thermal emission from cooling neutron stars, surface explosions, and gravity wave emissions are some promising areas for measurements of mass and radius; on the experimental side, heavy-ion collisions, giant dipole resonances, and parity-violating electron scattering are some promising techniques for measuring the density dependence of the pressure of nuclear matter. These efforts are complementary, and determining an EOS from the many disparate measurements is a challenging task.

This paper consists of two parts. In the first, we consider simultaneous mass and radius information from astrophysical observations of X-ray bursts and thermal emissions from quiescent low-mass X-ray binaries (LMXBs). We critically assess the mass and radius constraints determined from X-ray bursts that may reach the Eddington limit (Section 2; van Paradijs 1979, 1982; Paczyński & Anderson 1986; van Paradijs et al. 1990). Heretofore, these bursts have been interpreted assuming that the

photospheric radius is equal to the stellar radius at “touchdown,” when the effective temperature reaches a maximum (Özel 2006; Özel et al. 2009, 2010; Güver et al. 2010a, 2010b). If true, rather stringent constraints on mass and radius are predicted. Using the most probable values for the observed flux and angular emission area, however, does not result in real-valued masses and radii. Özel et al. (2010) argue for rejecting much of the observed phase space on this basis and thus obtain tight constraints on masses and radii. We show that this model is not internally consistent, but that consistency can be regained by relaxing the assumption concerning the effective photospheric radius. With this modification, the inferred neutron star radii moderately increase and confidence intervals for predicted masses and radii become substantially larger than those previously quoted (Özel 2006; Özel et al. 2009, 2010; Güver et al. 2010a, 2010b).

We then discuss (Section 3) mass and radius estimates from thermal emission from quiescent LMXBs. Neutron stars in quiescent LMXBs may be used to obtain angular emission areas, and thereby mass and radius information, from their quiescent thermal emission. In total, we have mass and radius constraints for six neutron stars: three bursting sources with photospheric radius expansion (PRE) bursts and three quiescent neutron star transients.

While not all of the uncertainties involved in constraining the masses and radii of neutron stars are under control, it is important to *quantify* the constraints on the EOS which are implied by the observations. In the second part of this paper (Section 4), we use a Bayesian analysis to combine these mass and radius constraints to determine empirical pressure–density and neutron star mass–radius relations. We include constraints to the EOS from causality, the observed minimum value of the neutron star maximum mass, and the observed maximum pulsar spin frequency. We employ a parameterized EOS (Section 4.2) that is compatible with laboratory measurements, and use it with a Markov Chain Monte Carlo (MC) algorithm to jointly

fit these mass–radius constraints (Section 4.3). We show, for the first time, using astrophysical observations alone, that values of the nuclear parameters such as the incompressibility  $K$ , bulk symmetry energy  $S_v$ , and the density dependence of the symmetry energy  $\gamma$ , all lie in ranges expected from nuclear systematics and laboratory experiments. Furthermore, our results imply that the most likely neutron star radius is relatively small, of order 11–12 km for neutron stars with masses near  $1.4 M_\odot$ , so that the predicted EOS is relatively soft in the density range 1–3 times the nuclear saturation density. Implications for the maximum mass sensitively depend on assumptions concerning X-ray burst models and are discussed in Section 4.4. In Section 5, we discuss astrophysical and nuclear physical implications of our results, and compare our methods and results with other studies.

## 2. MASS AND RADIUS CONSTRAINTS FROM PHOTOSPHERIC RADIUS EXPANSION BURSTS

Although a few dozen neutron star masses have been determined very accurately (to within a few percent) in binaries containing pulsars (for a recent compilation, see Lattimer & Prakash 2005), no radius information is available for these systems. For systems in which the neutron star accretes matter from a nearby companion, nuclear processes in the crust and envelope of the neutron star provide additional observables that can be used to constrain its mass and radius. Our discussion here initially follows that of Özel (2006), and is provided to establish a framework for the subsequent assessment of this method in Sections 2.1 and 2.2.

Type-I X-ray bursts are the result of thermally unstable helium (or in some cases, hydrogen) ignition in the accreted envelope of a neutron star (for a review, see Strohmayer & Bildsten 2004). The ignition generates a thermonuclear explosion that is observed as an X-ray burst with a rapid rise ( $\sim 1$  s) followed by a slower decay ( $\sim 10$ – $100$  s). With the discovery of significant spectral softening during some bursts, it quickly became apparent that significant radial expansion of the photosphere can occur during powerful X-ray bursts: if the burst is sufficiently luminous, radiation pressure drives the photosphere outward to larger radii, in some cases substantially so. About 20% of X-ray bursts show evidence for PRE (Galloway et al. 2008). The inference that radius expansion occurred spurred many (e.g., Paczyński 1983; Ebisuzaki et al. 1983) to construct models of extended, radiation-dominated neutron star envelopes. There is widespread agreement from these calculations that during a radius expansion burst, the flux at the photosphere approaches (to within a few percent) the Eddington value. The convective zone is expected to reach the photosphere during a powerful burst (Woosley et al. 2004; Weinberg et al. 2005) thereby polluting the accreted material with heavier nuclei synthesized during the burst.

During a typical PRE burst, the flux rapidly increases, peaks, and then decreases. While the flux  $F_\infty$  is near maximum, the blackbody temperature  $T_{\text{bb},\infty}$  at first decreases, then increases to a maximum before decreasing again. (The  $\infty$  subscript indicates that the quantities are observed at the Earth and therefore differ from their value in a reference frame local to the emission.) During this time, the normalized area  $F_\infty/T_{\text{bb},\infty}^4$  increases to a maximum value and then decreases as  $T_{\text{bb},\infty}$  increases. The point at which  $T_{\text{bb},\infty}$  reaches a maximum (and the normalized area typically stops decreasing and becomes constant) is thought to be when the photosphere “touches down” at the stellar radius. We shall denote the observed flux, measured at this time, as

$F_{\text{TD},\infty}$ . Following this point, the angular emission area remains roughly constant as both  $F_\infty$  and  $T_{\text{bb},\infty}$  slowly decrease. At the peak of the expansion, the low blackbody temperature puts much of the emitted flux below the bandpass for many X-ray instruments; in extreme cases this can create the appearance of a “precursor” burst (Hoffman et al. 1978; in’t Zand & Weinberg 2010). Damen et al. (1990) argued that to minimize systematic errors in determining the Eddington flux, the measurement should be made at touchdown, when the temperature is at a maximum and the photosphere has presumably just retreated to near the quiescent stellar radius.

At touchdown, the observed flux is expected to equal the *local*, i.e., as measured in a frame co-moving with the photosphere, Eddington value

$$F_{\text{TD},\infty} \simeq \frac{GMc}{\kappa D^2} \sqrt{1 - 2\beta(r_{\text{ph}})} \equiv F_{\text{Edd}} \sqrt{1 - 2\beta(r_{\text{ph}})}. \quad (1)$$

Here,  $\beta(r) = GM/(rc^2)$ ,  $\kappa$  is the opacity, and  $r_{\text{ph}}$  is the photospheric radius at the time this flux is evaluated. Özel (2006) argued that at touchdown, i.e., when  $T_{\text{bb}}$  reaches a maximum,  $r_{\text{ph}} = R$ . For clarity, when we refer to the Eddington flux in the remainder of the paper, we shall mean  $F_{\text{Edd}} \equiv GMc/(\kappa D^2)$ . This definition is independent of the stellar radius, and is a true limiting flux:  $F_{\text{TD},\infty} \leq F_{\text{Edd}}$ , with equality holding if  $r_{\text{ph}} \gg R$ . Finally, for Thomson scattering in a hydrogen–helium plasma,  $\kappa \approx 0.2(1 + X) \text{ cm}^2 \text{ g}^{-1}$ , where  $X$  is the mass fraction of hydrogen.

Galloway et al. (2008) examined a large sample of PRE bursts. They found that in all cases for which the inclination was not extremely high, the touchdown flux was within a factor of 1.6 of the peak flux, consistent with it occurring when the photosphere had retreated. The source EXO 0748–676, which was used in previous analysis (Özel 2006) because of its claimed redshift measurement (Cottam et al. 2002), has a high inclination (it is a “dipper”); as a result, the observed touchdown flux may be obscured by the disk, and indeed  $F_{\text{TD},\infty}$  is much less than the observed maximum flux for this source. The distance to EXO 0748–676 is also not well known, and for these reasons we omit this source in our analysis below.

In the latter part of the burst, the ratio  $F_\infty/T_{\text{bb},\infty}^4$  is observed to be roughly constant. This allows one to define a normalized angular surface area,

$$A \equiv \frac{F_\infty}{\sigma T_{\text{bb},\infty}^4} = f_c^{-4} \left( \frac{R}{D} \right)^2 (1 - 2\beta)^{-1}. \quad (2)$$

Here,  $F_\infty$  and  $T_{\text{bb},\infty}$  are the flux and blackbody temperature as measured by a distant observer in the late phase of the burst, when  $A$  is roughly constant,  $\beta = GM/(Rc^2)$  is the compactness,  $D$  is the distance to the source, and  $f_c \equiv T_{\text{bb}}/T_{\text{eff}}$  is a color-correction factor that accounts for the departure of the spectrum from a blackbody.

If a distance to the star can be estimated with sufficient precision, the observed touchdown flux (when the blackbody temperature reaches a maximum following the PRE) and the inferred apparent angular area measured late in the burst can be converted into an estimate of the stellar mass and radius. It has been claimed that  $1\sigma$  uncertainties of less than 10% in both mass and radius are possible (Özel 2006; Özel et al. 2009, 2010). Systematic uncertainties not included in the analyses of Özel (2006) and Özel et al. (2009) include the composition of the accreted material and the effects of the neutron star

**Table 1**  
Observational Values for Type-I X-ray Burst Sources Used in this Paper

Quantity	EXO 1745–248	4U 1608–522	4U 1820–30
$D$ (kpc)	$6.3 \pm 0.6$	$5.8 \pm 2.0^a$	$8.2 \pm 0.7^b$
$A$ ( $\text{km}^2 \text{kpc}^{-2}$ )	$1.17 \pm 0.13$	$3.246 \pm 0.024$	$0.9198 \pm 0.0186$
$F_{\text{TD},\infty}$ ( $10^{-8} \text{ erg cm}^{-2} \text{s}^{-1}$ )	$6.25 \pm 0.2$	$15.41 \pm 0.65$	$5.39 \pm 0.12$
$\alpha^c$	$0.131 \pm 0.017$	$0.179 \pm 0.062$	$0.166 \pm 0.015$
$\gamma$ (km) <sup>c</sup>	$101.7 \pm 11.8$	$114.5 \pm 4.9$	$92.7 \pm 2.8$
$R_\infty = \alpha\gamma$ (km) <sup>c</sup>	$13.4 \pm 2.0$	$20.5 \pm 7.1$	$15.4 \pm 1.4$

**Notes.** See the [Appendix](#) for details about how the uncertainties were determined.

<sup>a</sup> The distance distribution for 4U 1608–522 was cut off below 3.9 kpc.

<sup>b</sup> The distance uncertainty for 4U 1820–30 was approximated by Güver et al. (2010b) as a boxcar with half-width 1.4 kpc.

<sup>c</sup> Assuming  $f_c = 1.4$  and  $X = 0$  with  $\Delta f_c = \Delta X = 0$ . Errors are computed assuming uncorrelated Gaussian errors for  $D$ ,  $F_{\text{TD},\infty}$ , and  $A$ .

**References.** (1) Özel 2006; (2) Özel et al. 2009; (3) Güver et al. 2010a; (4) Güver et al. 2010b.

atmosphere on the spectral shape, although these are included in later analyses (Güver et al. 2010a; Özel et al. 2010). A key question is whether the value of  $\beta(r_{\text{ph}})$  in Equation (1), which is determined by  $r_{\text{ph}}$ , is the same as the value of  $\beta$  in Equation (2). In the following discussion, we shall first assume that these  $\beta$  values are the same, i.e.,  $r_{\text{ph}} = R$ , as would be the case if the photosphere has indeed just retreated to the stellar radius. We will demonstrate that for EXO 1745–248, 4U 1608–522, and 4U 1820–30 the most probable observed values of  $A$  and  $F_{\text{Edd},\infty}$  do not lead to real-valued solutions for  $M$  and  $R$ . Indeed, Özel et al. (2010) note that forcing a real-valued solution for mass and radius by MC sampling within the probability distributions of the observables  $F_{\text{TD},\infty}$ ,  $A$ , and  $D$  reduces the uncertainties in the mass and radius to values smaller than those of the measurements. We shall explore in Section 2.2 a different interpretation, which is that  $r_{\text{ph}} > R$  when  $F_{\text{TD},\infty}$  is evaluated, so that  $F_{\text{TD},\infty} \lesssim F_{\text{Edd}}$ . We show that relaxing the assumption  $r_{\text{ph}} = R$  generally yields real-valued solutions for  $M$  and  $R$  for the most probable values of the observables.

We combine the observed quantities  $F_{\text{TD},\infty}$  and  $A$ , along with a measurement of the distance  $D$  and theoretical estimates of  $f_c$  and  $\kappa$ , into two parameters,

$$\alpha \equiv \frac{F_{\text{TD},\infty}}{\sqrt{A}} \frac{\kappa D}{c^3 f_c^2}, \quad (3)$$

$$\gamma \equiv \frac{Ac^3 f_c^4}{F_{\text{TD},\infty} \kappa}. \quad (4)$$

If we then make the assumption, following Özel (2006), that  $F_{\text{TD},\infty} = F_{\text{Edd}}\sqrt{1-2\beta}$  in Equation (1), we find

$$\alpha = \beta(1-2\beta), \quad (5)$$

$$\gamma = \frac{R}{\beta(1-2\beta)^{3/2}}. \quad (6)$$

Solving Equation (5) for  $\beta$ , we then solve Equation (6) for the radius and mass:

$$\beta = \frac{1}{4} \pm \frac{1}{4} \sqrt{1-8\alpha}, \quad (7)$$

$$R = \alpha\gamma\sqrt{1-2\beta}, \quad (8)$$

$$M = \frac{\beta R c^2}{G}. \quad (9)$$

Note that  $\gamma$  is independent of  $D$ . An important consequence of Equation (7) is that for both  $M$  and  $R$  to be real, we must have  $\alpha \leq 1/8$ . Since  $\alpha$  is determined, however, from the observables  $F_{\text{TD},\infty}$ ,  $A$ , and  $D$ , as well as the estimated parameters  $\kappa$  and  $f_c$ , the inferred value of  $\alpha$  does not necessarily satisfy this mathematical limit. *This condition serves as a check on the validity of the assumptions made in the modeling of the radius expansion bursts.*

### 2.1. Monte Carlo Analysis of Photospheric Radius Expansion Burst Data

Observational information for three Type-I X-ray bursters with PRE bursts (Özel et al. 2009; Güver et al. 2010a, 2010b) is presented in Table 1, along with associated uncertainties. We have reexamined the uncertainties for each object as described in the [Appendix](#); in some cases our values for the uncertainties differ from those used previously.

We first fix  $f_c = 1.4$  and  $X = 0$  as was done in previous work for EXO 1745–248 (Özel et al. 2009). We observe in this case from Table 1 that no real-valued solution of Equations (7)–(9) is possible for any of the sources because  $\alpha > 1/8$  for the central values of the observables. Moreover, it is not consistent with X-ray burst models to fix the color-correction factor to  $f_c = 1.4$  and the hydrogen abundance to  $X = 0$ , and indeed these restrictions were relaxed in subsequent analyses of 4U 1608–522 and 4U 1820–30 (Güver et al. 2010a, 2010b). Atmosphere models (Madej et al. 2004) suggest a range  $1.33 < f_c < 1.81$ ; these are consistent with earlier calculations (London et al. 1986; Ebisuzaki & Nakamura 1988). The largest values of  $f_c$  are approached as the flux approaches the Eddington limit. In the tail of the burst, the flux is lower and  $f_c$  does not vary strongly. We choose to select the value of  $f_c$  in our MC analysis from a boxcar distribution centered at  $f_c = 1.4$  with an uncertainty of 0.07. This selection is comparable to the boxcar distribution with  $f_c = 1.35 \pm 0.05$  used previously (Güver et al. 2010a, 2010b). (In the following, we denote a boxcar uncertainty in  $X$  as  $\Delta X$  and a Gaussian uncertainty with  $\sigma_X$ .) In addition, as described in Appendices A.1 and A.2, we find insufficient information from the observations to exclude any possible values of  $X$  for EXO 1745–248 and 4U 1608–522, so we choose a uniform distribution with  $0 < X < 0.7$ , which is also assumed by Güver et al. (2010a, 2010b). The source 4U 1820–30 is an ultracompact and accretes He-rich fuel (see Appendix A.3).



**Table 2**

Comparison of Monte Carlo Realizations for PRE Bursts Employing Data from Table 1

Quantity	EXO 1745–248	4U 1608–522	4U 1820–30
$F_{\text{TD},\infty} = F_{\text{Edd}}[1 - 2\beta(R)]^{1/2}; \alpha$ unrestricted			
$\hat{\alpha}$	$0.165^{+0.045}_{-0.028}$	$0.229^{+0.054}_{-0.038}$	$0.167^{+0.018}_{-0.017}$
$\hat{\gamma}$ (km)	$70.4^{+19.2}_{-14.7}$	$80.2^{+18.8}_{-15.5}$	$80.9^{+21.2}_{-3.56}$
$\hat{R}_{\infty}$ (km)	$13.2^{+1.7}_{-1.6}$	$20.5^{+5.7}_{-5.5}$	$15.3^{+1.7}_{-1.5}$
$F_{\text{TD},\infty} = F_{\text{Edd}}[1 - 2\beta(R)]^{1/2}; \alpha < 1/8$ restriction			
$\hat{\alpha}$	$0.122^{+0.003}_{-0.007}$	$0.123^{+0.003}_{-0.005}$	$0.123^{+0.003}_{-0.004}$
$\hat{\gamma}$ (km)	$107.9^{+14.2}_{-14.2}$	$127.1^{+8.0}_{-7.9}$	$109.3^{+5.3}_{-8.1}$
$\hat{R}_{\infty}$ (km)	$12.7^{+1.6}_{-1.6}$	$15.2^{+0.85}_{-0.81}$	$13.2^{+0.78}_{-1.1}$
Points accepted	4.4%	0.24%	0.44%
$F_{\text{TD},\infty} = F_{\text{Edd}}[1 - 2\beta(R)]^{1/2}; \alpha < 1/8$ ; original inputs from Özel et al.			
$\hat{\alpha}$	$0.122^{+0.003}_{-0.003}$	$0.122^{+0.003}_{-0.003}$	$0.124^{+0.001}_{-0.001}$
$\hat{\gamma}$ (km)	$109.0^{+4.2}_{-4.2}$	$113.1^{+5.0}_{-5.0}$	$104.0^{+1.8}_{-1.8}$
$\hat{R}_{\infty}$ (km)	$13.3^{+0.4}_{-0.4}$	$13.8^{+0.5}_{-0.5}$	$12.9^{+0.2}_{-0.2}$
Points accepted	13%	0.18%	$1.5 \times 10^{-6}\%$
$F_{\text{TD},\infty} = F_{\text{Edd}}; \alpha < 3^{-3/2} = 0.192$ restriction			
$\hat{\alpha}$	$0.165^{+0.026}_{-0.018}$	$0.180^{+0.012}_{-0.023}$	$0.167^{+0.016}_{-0.016}$
$\hat{\gamma}$ (km)	$79.0^{+17.2}_{-12.4}$	$97.0^{+15.4}_{-14.4}$	$91.0^{+13.8}_{-10.6}$
$\hat{R}_{\infty}$ (km)	$13.1^{+1.8}_{-1.6}$	$15.3^{+2.8}_{-1.3}$	$15.0^{+1.8}_{-1.4}$
Points accepted	65%	15%	91%
$F_{\text{Edd}}[1 - 2\beta(R)]^{1/2} < F_{\text{TD},\infty} < F_{\text{Edd}}; q^3 + p^2 < 0$ restriction			
$\hat{\alpha}$	$0.143^{+0.022}_{-0.018}$	$0.155^{+0.018}_{-0.019}$	$0.158^{+0.014}_{-0.015}$
$\hat{\gamma}$ (km)	$87.1^{+17.5}_{-13.8}$	$103.0^{+16.6}_{-13.6}$	$104.8^{+5.6}_{-17.0}$
$\hat{R}_{\infty}$ (km)	$13.0^{+1.8}_{-1.6}$	$15.3^{+2.3}_{-1.4}$	$15.0^{+1.6}_{-1.6}$
Points accepted	32%	5.8%	37%

**Notes.** In the third group, we use the values and distributions of  $F_{\text{TD}}$ ,  $A$ ,  $D$ ,  $f_c$ , and  $X$  from Özel et al. (2009), Güver et al. (2010a), and Güver et al. (2010b). For all other entries, we use  $0 < X < 0.7$  for the hydrogen mass fraction, except for 4U 1820–30, for which  $X = 0$  and we use  $1.33 < f_c < 1.47$  for the color-correction factor.

If values of  $f_c$  and  $X$  or the observables  $F_{\text{TD},\infty}$ ,  $A$ , or  $D$  are selected at random from their respective probability distributions, some combinations will satisfy the condition  $\alpha < 1/8$ . In this way, using only these acceptable combinations, the most probable values  $\hat{\alpha}$  and  $\hat{\gamma}$  can be established using MC sampling. (Here and below, we define  $\hat{X}$  to be the most probable value of  $X$  obtained from an MC simulation, and the uncertainties on this quantity are determined by selecting the region surrounding the most probable value that includes 68% of the total MC weight.) Values for  $M$  and  $R$ , and their uncertainties, can then be determined from  $\hat{\alpha}$  and  $\hat{\gamma}$  using Equations (7)–(9). But the fraction of accepted realizations is then very small as shown in Table 2. The entries in the first group of this table give the most probable values  $\hat{\alpha}$ ,  $\hat{\gamma}$ , and  $\hat{R}_{\infty}$  using  $r_{\text{ph}} = R$  and values for  $F_{\text{TD},\infty}$ ,  $A$ , and  $D$  from their probability distributions summarized in Table 1 and, for  $f_c$  and  $X$ , from previous discussion. For each quantity, the uncertainty is determined by creating a histogram for the indicated MC realizations, sorting the bins by decreasing weight, and selecting the range which encloses 68% of the sum of all bins. We identify  $R_{\infty} = [F_{\infty}/(4\pi\sigma T_{\text{eff},\infty}^4)]^{1/2} = R/\sqrt{1 - 2\beta} = \alpha\gamma$  and impose no a priori restriction for the value of  $\alpha$ . The most probable value of  $\alpha$ ,  $\hat{\alpha}$ , is observed to be approximately a factor  $1 + \bar{X}$  larger than the value of  $\alpha$  in Table 1, where  $\bar{X}$  is the average value

of  $X$  in its assumed range, i.e., 1.35 for EXO 1745–248 and 4U 1608–522, and 1.0 for 4U 1820–30. For all three sources,  $\hat{\alpha} > 1/8$  by several standard deviations.

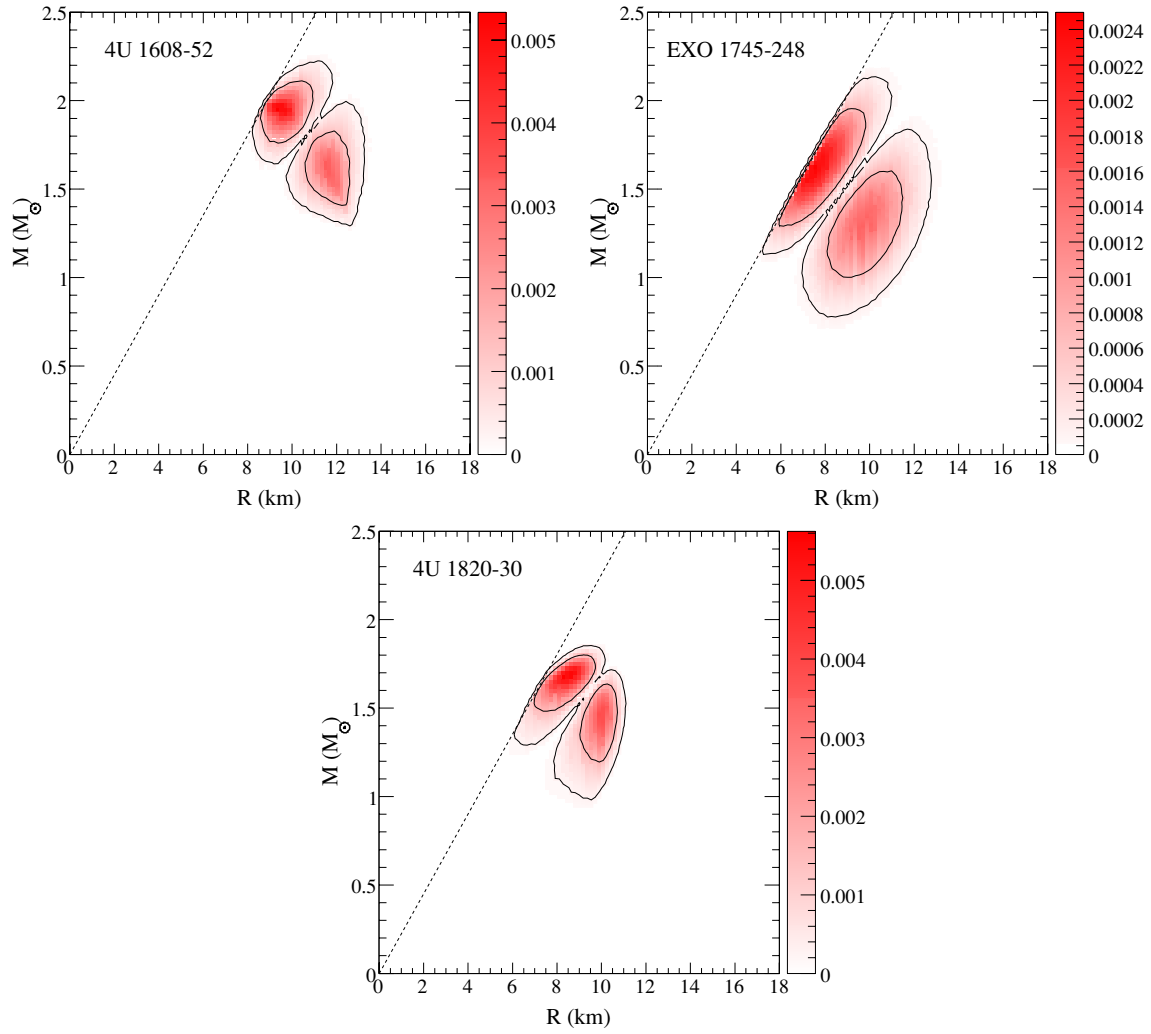
In the second group of Table 2, we repeat the analysis, but this time only accept realizations for which  $\alpha \leq 1/8$ . Note that at most 4% of the realizations are accepted. This implies, at a minimum, that the assumptions in this model are incomplete. The most probable value for  $\alpha$  decreases and now lies approximately  $1\sigma$  below the value  $1/8$ , and the size of confidence interval for  $\hat{\alpha}$  is now significantly reduced compared to the unrestricted case, by factors of 4–18. *The net effect is to pre-select the value  $1/8$  for  $\hat{\alpha}$  irrespective of the observed values of  $F_{\text{TD},\infty}$ ,  $A$ , and  $D$ .* Another consequence of the selective rejection of most of the MC realizations is to increase the most probable value of  $\gamma$  and decreases the most probable value of  $R_{\infty}$ , and to greatly decrease their uncertainties; the latter result was already noted by Özel et al. (2010). In addition, the resulting values of  $\hat{\gamma}$  and  $\hat{R}_{\infty}$  for the different sources are also “herded” into similar values (Özel et al. 2009; Güver et al. 2010a, 2010b). The third group summarizes the MC results obtained using the exact same observational inputs found in those references. Note that for 4U 1820–30, only about 1 realization out of 100 million is now accepted! The larger acceptance rate for EXO 1745–248 is due to the assumption that  $X = 0$  which gives the smallest possible  $\alpha$ . Analyses of X-ray bursts with this model result in certain values for  $M$  and  $R$  that are nearly independent of  $\alpha$  and  $\gamma$ , and are therefore almost completely independent of the observables  $F_{\text{TD},\infty}$ ,  $A$ , and  $D$ , which seems unrealistic. The fact that only a small fraction of realizations are accepted may indicate that the underlying model contains systematic errors or is unphysical, a point we shall explore in the next section.

Figure 1 displays the MC probability distributions for the masses and radii of EXO 1745–248, 4U 1608–522, and 4U 1820–30 as determined from  $\alpha$  and  $\gamma$  following Equations (7)–(9), and with the restriction  $\alpha \leq 1/8$ . There are two peaks in the distributions because of the quadratic in Equation (7). We also impose that  $\beta < 1/2.94 \approx 0.34$  (Glendenning 1992), which is based on requiring a subluminal sound speed throughout the star (see also Lattimer & Prakash 2007). This causes the rejection of a small fraction of realizations from the higher-redshift region. For all three sources, our confidence intervals are larger than computed in previous works (Özel et al. 2009; Güver et al. 2010a, 2010b). The origin of this distinction is because we use larger variations  $f_c$  and, for EXO 1745–248, in  $X$ , and we employ a different uncertainty in  $D$  for 4U 1820–30. A detailed discussion of the treatment of the uncertainties in the observables for each object is given in the Appendix.

When using a Monte Carlo scheme to determine uncertainties, we find that the two error ranges in Figure 1 are equally populated, while Özel et al. (2009), Güver et al. (2010a, 2010b), and Özel et al. (2010), transforming probabilities using a Jacobian, indicate a much higher probability for the higher redshift solution. This difference is caused by a numerical error in their Jacobian (F. Özel 2010, private communication); when the correct Jacobian is used, both integration methods agree.

## 2.2. Alternate Interpretations of the Location of the Photospheric Radius at Touchdown

The lack of real-valued solutions for  $M$  and  $R$  for the most probable values of the observables, and indeed, the rejection of the vast majority of MC realizations, motivates us to consider another possibility; namely, that at “touchdown”



**Figure 1.** Mass–radius probability distributions for Type-I X-ray bursts assuming that the photospheric radius and the stellar radius are identical. The causal limit  $\beta = 1/2.94$  is indicated with a dashed line. These plots correspond to the results shown in the second group in Table 2. The solid curves indicate the 68% and 95% confidence boundaries while the shading level reflects the relative probabilities. All distributions,  $P_i$ , are normalized so that  $\int P_i dM dR = 1$ . (A color version of this figure is available in the online journal.)

the photosphere is still extended. To explore this situation, we first consider the extreme possibility that  $r_{\text{ph}} \gg R$  at the point identified as touchdown from the maximum in  $T_{\text{bb},\infty}$ . In this case,  $F_{\text{TD},\infty} = F_{\text{Edd}}$  and is independent of the stellar radius  $R$ . With this assumption,  $\alpha$  (Equation (3)) and  $\gamma$  (Equation (4)) are now related to  $\beta$  and  $R$  via

$$\alpha = \beta \sqrt{1 - 2\beta}, \quad (10)$$

$$\gamma = \frac{R}{\beta(1 - 2\beta)}. \quad (11)$$

Defining a quantity  $\theta = \cos^{-1}(1 - 54\alpha^2)$ , the expressions for the compactness, radius, and mass are then

$$\beta_1 = \frac{1}{6} [1 + \sqrt{3} \sin(\theta/3) - \cos(\theta/3)], \quad (12)$$

$$\beta_2 = \frac{1}{6} [1 + 2 \cos(\theta/3)], \quad (13)$$

$$R = \alpha \gamma \sqrt{1 - 2\beta_{1,2}}, \quad (14)$$

$$M = \frac{c^2}{G} \alpha^2 \gamma. \quad (15)$$

Obviously,  $M$  is real for all  $\alpha, \gamma > 0$ . For  $\alpha < 3^{-3/2} \simeq 0.192$ ,  $\theta$  is real and there are three real roots for  $\beta$  and  $R$ . Only two of these,  $0 \leq \beta_1 \leq 1/3$  and  $1/3 \leq \beta_2 \leq 1/2$ , are physically meaningful: the other root is negative. When  $\alpha > 3^{-3/2}$  there is one real root for  $\beta$  and two imaginary ones, but the real root is negative.

From the top group in Table 2, we can see that both 4U 1820–30 and EXO 1745–248 have most probable values of  $\alpha$  that satisfy the constraint for positive real values of  $\beta$  and  $R$ , and 4U 1608–522 lies less than  $1\sigma$  above this limit. Therefore, we now find that a much larger fraction of the MC realizations are accepted when selecting values for  $F_{\text{TD},\infty}$ ,  $A$ ,  $D$ ,  $f_c$ , and  $X$  from their probability distributions. This is shown in the fourth group of Table 2, for which we use the model given in Equations (10) and (11) and impose the restriction  $\alpha < 0.192$ . In contrast to the case in which  $r_{\text{ph}} = R$ , the uncertainties in  $\hat{\alpha}$  and  $\hat{\gamma}$  are not as strongly diminished. Moreover, the values for  $\hat{\alpha}$  are no longer nearly the same for the three sources. While in principle each accepted realization results in two  $M, R$  values, one corresponding to  $\beta_1$  and the other to  $\beta_2$ , nearly all

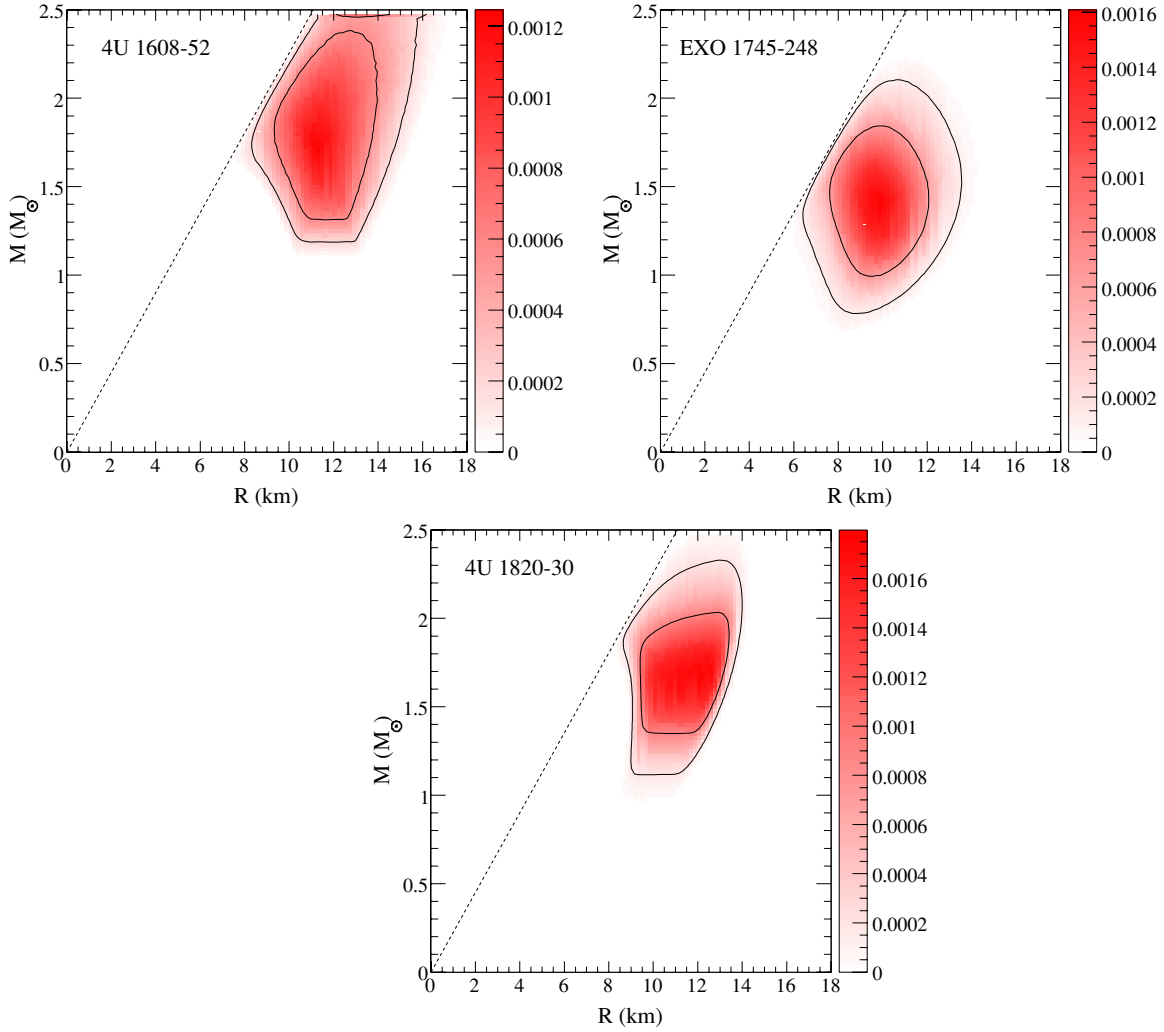


**Figure 2.** Mass–radius probability distributions for Type-I X-ray bursts assuming that  $r_{\text{ph}} \gg R$ . The causal limit  $\beta = 1/2.94$  is indicated with a dashed line. These plots correspond to the results shown in the fourth group in Table 2. The solid curves indicate the 68% and 95% confidence boundaries while the shading level reflects the relative probabilities. All distributions,  $P_i$ , are normalized so that  $\int P_i dM dR = 1$ .

(A color version of this figure is available in the online journal.)

the  $\beta_2$  realizations are rejected on the basis of causality when  $\beta_2 > 1/2.94$ . Figure 2 displays the probability distributions for the fourth group of runs listed in Table 2, as well as their 68% and 95% contours. The error contours are larger than those shown in Figure 1 and considerably larger than determined previously (Özel 2006; Özel et al. 2009; Güver et al. 2010a, 2010b).

It is perhaps unphysical to make the extreme assumption  $r_{\text{ph}} \gg R$  when  $T_{\text{eff}}$  reaches a maximum. But because of the relative consistency of the solutions and the much larger fraction of MC points accepted in this case, it seems reasonable to consider the possibility that at touchdown, that is, when  $T_{\text{bb},\infty}$  reaches a maximum and the normalization reaches a minimum, the photospheric radius may in fact be larger than the quiescent stellar radius. We can write  $\alpha = \beta\sqrt{1 - 2\beta}\sqrt{1 - h\beta}$ , where  $\beta_{\text{ph}} = GM/(r_{\text{ph}}c^2) < \beta$ . Defining the quantity  $h = 2R/r_{\text{ph}}$ , the quantities  $\alpha$  and  $\gamma$  now become

$$\alpha = \frac{F_{\text{Edd}}}{\sqrt{A}} \frac{\kappa D}{c^3 f_c^2} = \beta\sqrt{1 - 2\beta}\sqrt{1 - h\beta}, \quad (16)$$

$$\gamma = \frac{Ac^3 f_c^4}{F_{\text{Edd}} \kappa} = \frac{R}{\beta(1 - 2\beta)\sqrt{1 - h\beta}}. \quad (17)$$

Note that  $R_\infty = \alpha\gamma$  remains unchanged. Equation (16) is a quartic equation for  $\beta$ . Two positive real solutions for  $\beta$  exist when  $q^2 + p^3 < 0$ , where

$$p = \frac{1}{6h} \left( \alpha^2 - \frac{1}{24h} \right), \quad (18)$$

$$q = -\frac{1}{12h} \left( \frac{1}{144h^2} + 3a\alpha^2 \right), \quad (19)$$

$$a = \frac{1}{6h} \left( 1 - \frac{3(2+h)^2}{16h} \right); \quad (20)$$

otherwise the only real solution is negative. Defining the quantities

$$\theta = \cos^{-1} \left[ \left( \frac{q}{-p} \right)^{3/2} \right], \quad (21)$$

$$v = 2\sqrt{-p} \cos(\theta/3), \quad (22)$$

$$w = \sqrt{2v - 2a}, \quad (23)$$

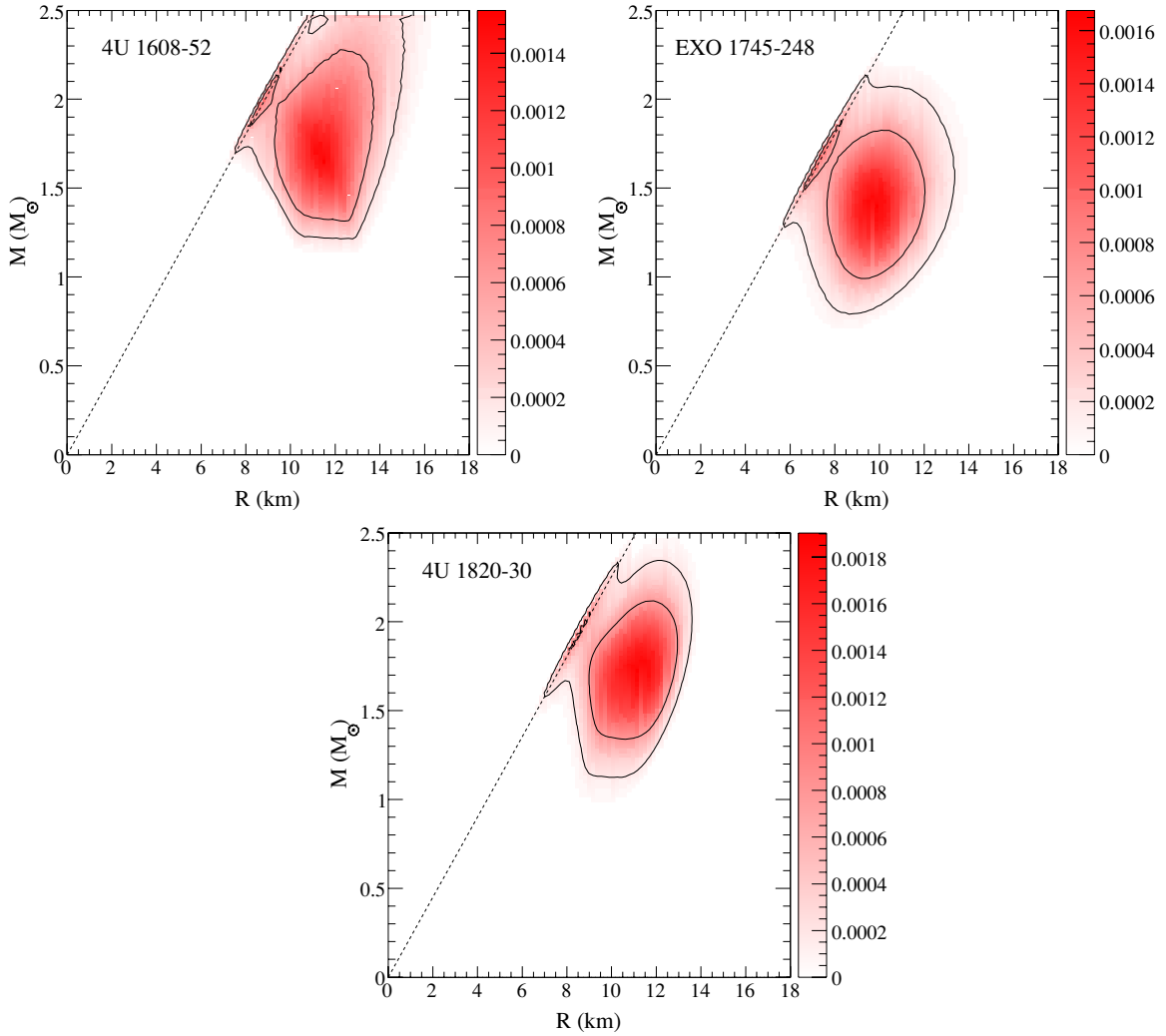


**Figure 3.** Mass–radius probability distributions for Type-I X-ray bursts assuming a uniform distribution in  $h = 2R/r_{\text{ph}}$ . The shadings and lines have the same meaning as in Figure 2.

(A color version of this figure is available in the online journal.)

$$z_{\pm} = - \left( 2v + 4a \pm \frac{2b}{w} \right), \quad (24)$$

$$b = \frac{(2+h)^2}{8h^2} \left[ 1 - \frac{2+h}{8h} \right], \quad (25)$$

the two solutions for  $\beta$  with values in the range  $0 \leq \beta \leq 0.5$  are

$$\beta_{\pm} = \frac{2+h}{8h} \pm \frac{w - \sqrt{z_{\pm}}}{2}, \quad (26)$$

where the sign has the same sense in the two occurrences.

Figure 3 displays the resulting probability distributions assuming that  $h$  is uniformly distributed in the range  $0 < h < 2$ , i.e.,  $R < r_{\text{ph}} < \infty$ . The error contours are much larger than those determined in the  $h = 2$  ( $r_{\text{ph}} = R$ ) case and slightly larger than those in the  $h = 0$  ( $r_{\text{ph}} \gg R$ ) cases. Most of the solutions for  $\beta_+$  are rejected because they lead to acausal combinations of  $M$  and  $R$ . The fifth group in Table 2 presents the associated values of  $\alpha$ ,  $\gamma$ , and  $R_{\infty}$ . These results are nearly identical to those of Figure 2 because small values of the photospheric radius are strongly disfavored by the requirement that the masses and radii are real valued. We will therefore use the  $r_{\text{ph}} \gg R$  probability

distributions in  $M$  and  $R$  for the Bayesian estimation of the EOS in Section 4, and note that these results will be essentially identical to what one would obtain without assuming a particular value for the radius of the photosphere, as long as it is not a priori assumed to be equal to  $R$ .

Using the number of accepted MC realizations as a guide, we can also obtain an estimate for the lower limit of the location of the photosphere at touchdown. As is common in Bayesian analysis, we use the ratio 0.1 as a guide; models for which the fraction of accepted realizations is less than 0.1 are rejected. This implies that  $r_{\text{ph}} > 5.0R$  for 4U 1608–522,  $r_{\text{ph}} > 1.1R$  for EXO 1745–248, and  $r_{\text{ph}} > 1.4R$  for 4U 1820–30. This analysis appears to strongly disfavor an interpretation of the touchdown radius  $r_{\text{ph}} = R$  and we find it likely that the photospheric radius is extended at touchdown. At the same time, there is little difference between the results assuming  $h = 0$  or a uniform range  $0 < h < 2$ . It would then seem justified that we, in our remaining analysis, reject the interpretation  $r_{\text{ph}} = R$ , and make use of the  $r_{\text{ph}} \gg R$ ,  $h = 0$  interpretation. Nonetheless, we will also include results for the  $r_{\text{ph}} = R$  interpretation in the work below for comparison to previous studies. We will show that some aspects of the EOS constraints are dependent on whether one assumes that  $r_{\text{ph}} = R$  or  $r_{\text{ph}} \gg R$ .

### 3. MASS AND RADIUS CONSTRAINTS FROM THERMAL SPECTRA

The masses and radii of isolated neutron stars or ones in transient LMXBs can be inferred from spectral modeling if their distances are accurately determined. Relatively accurate distances are known for several accreting neutron star transients located in globular clusters. Although the uncertainties for any individual source are large, it is productive to use the ensemble of observations to improve constraints on the dense matter EOS. In addition, future mass and radius measurements from thermal sources are expected to tighten such constraints further.

Many neutron stars are in transients, for which the accretion of matter proceeds intermittently, with episodes of accretion separated by long periods of quiescence. While the neutron star accretes, compression of matter in the crust induces nuclear reactions (Haensel & Zdunik 1990) that release heat. When the accretion ceases, the heated crust cools, resulting in an observable thermal luminosity (Brown et al. 1998). Because the timescale for heavier nuclei to sink below the photosphere is short ( $\sim 10$  s; Bildsten et al. 1992), and these systems show no evidence for a significant magnetic field, such as pulsations or cyclotron spectral features, the spectra can be fitted with well-understood unmagnetized hydrogen atmosphere spectra (Zavlin et al. 1996; Rutledge et al. 1999; Heinke et al. 2006). As a result, the observed X-ray spectra can be used to reliably infer an apparent angular emitting area, and, possibly, the surface gravity (Heinke et al. 2006). Such objects with accurately determined distances (such as those in globular clusters) can be used to estimate masses and radii.

The spectra of isolated cooling neutron stars with well-determined distances, such as RX J1856–3754 discovered by Walter et al. (1996), have a much larger signal to noise than those of neutron star transients. The interpretation of their spectra is complicated, however, by the potentially strong magnetic field. The distance to RX J1856–3754 has been controversial. Walter & Lattimer (2002) gave a parallax distance  $D = 117 \pm 12$  pc based on *Hubble Space Telescope* (*HST*) observations from 1996–1998, but van Kerkwijk & Kaplan (2007) later found  $D = 161 \pm 16$  pc using new *HST* data from 2002 to 2004. Recently, Walter et al. (2010) reanalyzed the new data and found  $D = 122 \pm 13$  pc, in good agreement with their older estimate. A multi-wavelength spectral fit by Pons et al. (2002) for non-magnetic heavy element atmospheres (which they argued gave the best fits to the X-ray and optical spectra of RX J1845–3754) yielded  $R_\infty/D = 0.13 \pm 0.01$  km pc $^{-1}$  and  $0.3 < z < 0.4$ . Burwitz et al. (2001) argued, however, that these models predict spectral features such as absorption edges that are not apparent in the data. In addition, the existence of a bow shock (van Kerkwijk & Kulkarni 2001) and the detection of pulsations in the X-ray flux (Tiengo & Mereghetti 2007) and their period derivative (van Kerkwijk & Kaplan 2008) imply this star has a magnetic field of order  $10^{13}$  G. Nevertheless, there could be many reasons why spectral features are washed out from a rotating, highly magnetized, object. A two-temperature blackbody model, in which the X-ray flux is primarily emitted by a high-temperature region and the optical flux by a low-temperature region, gives  $R_\infty/D \simeq 0.14$  km pc $^{-1}$ , approximately the same value determined by Pons et al. (2002) and Burwitz et al. (2003). Motivated by the large distance determined by van Kerkwijk & Kaplan (2007), which implied radii incompatible with neutron star equations of state, Ho et al. (2007) developed a magnetized neutron star atmosphere model with a condensed surface and a trace amount of H remaining in

the atmosphere. This model resulted in  $R_\infty/D \simeq 0.12$  km pc $^{-1}$ . The origin of the trace H in the atmosphere is unknown, and its mass must be finely tuned to explain the magnitude of the optical flux. The analysis of Pons et al. (2002) coupled with the confirmed distance determination of Walter et al. (2010) yields  $M = 1.7 \pm 0.3 M_\odot$  and  $R = 11.5 \pm 1.2$  km, but this model neither accounts for a large magnetic field or the observed lack of spectral lines. Because of this, we do not include this source in our baseline results although we have performed a separate analysis to determine if our results would be appreciably affected.

Some of the strongest constraints on properties of transient neutron stars are for X7 in the globular cluster 47 Tuc (Heinke et al. 2006), and for the neutron stars in the globular clusters  $\omega$  Cen and M13 (Webb & Barret 2007). The 99% contours which define the  $M$  and  $R$  values inferred by the atmosphere models in Figure 8 of Webb & Barret (2007) and the 68%, 90%, and 99% contours inferred by the atmosphere models in Figure 2 of Heinke et al. (2006) are shown in Figure 4. For use in constraining the EOS, we need to create probability distributions for these observations in the  $(M, R)$  plane. While one can roughly represent the published constraints on  $M$  and  $R$  in terms of a single constraint on  $R_\infty$ , this is accurate only for smaller masses. To construct a better representation of the data, we first note that the likelihood contours are nearly perpendicular to lines emanating from the origin of the  $M, R$  plane. To construct a probability distribution, we assume that the probability is distributed as a Gaussian with a width determined by the spacing of the contours across a line going through the origin. Figure 4 shows a comparison between the resulting probability distributions used in this work and contours obtained in the original references.

### 4. APPLICATION OF STATISTICAL METHODS TO CONSTRAINTS ON THE EOS

As is clear from the preceding discussion, not all of the uncertainties involved in constraining the masses and radii of neutron stars are under control. Nevertheless, it is interesting to understand what these observations may imply for the EOS. Furthermore, it is important to *quantify* their implications for the EOS in order to motivate future observational work that will reduce these uncertainties.

In this section, we apply a Bayesian analysis to the data described above. We will first briefly review the formalism (Section 4.1), and then develop (Section 4.2) a general parameterization of the EOS. The output probability distribution for the EOS parameters and the EOS itself are presented in Section 4.3. The most probable masses and radii are presented in Section 4.4. Even though the results of Section 2 strongly suggest that  $r_{\text{ph}} = R$  is disfavored, we include results for both  $r_{\text{ph}} = R$  and  $r_{\text{ph}} \gg R$  to simplify comparison to previous studies.

#### 4.1. Bayesian Analysis

Bayes theorem can be formulated as (see, e.g., Grinstead & Snell 1997)

$$P(\mathcal{M}|D) = \frac{P(D|\mathcal{M})P(\mathcal{M})}{P(D)}, \quad (27)$$

where  $P(\mathcal{M})$  is the prior probability of the model  $\mathcal{M}$  without any information from the data  $D$ ,  $P(D)$  is the prior probability of



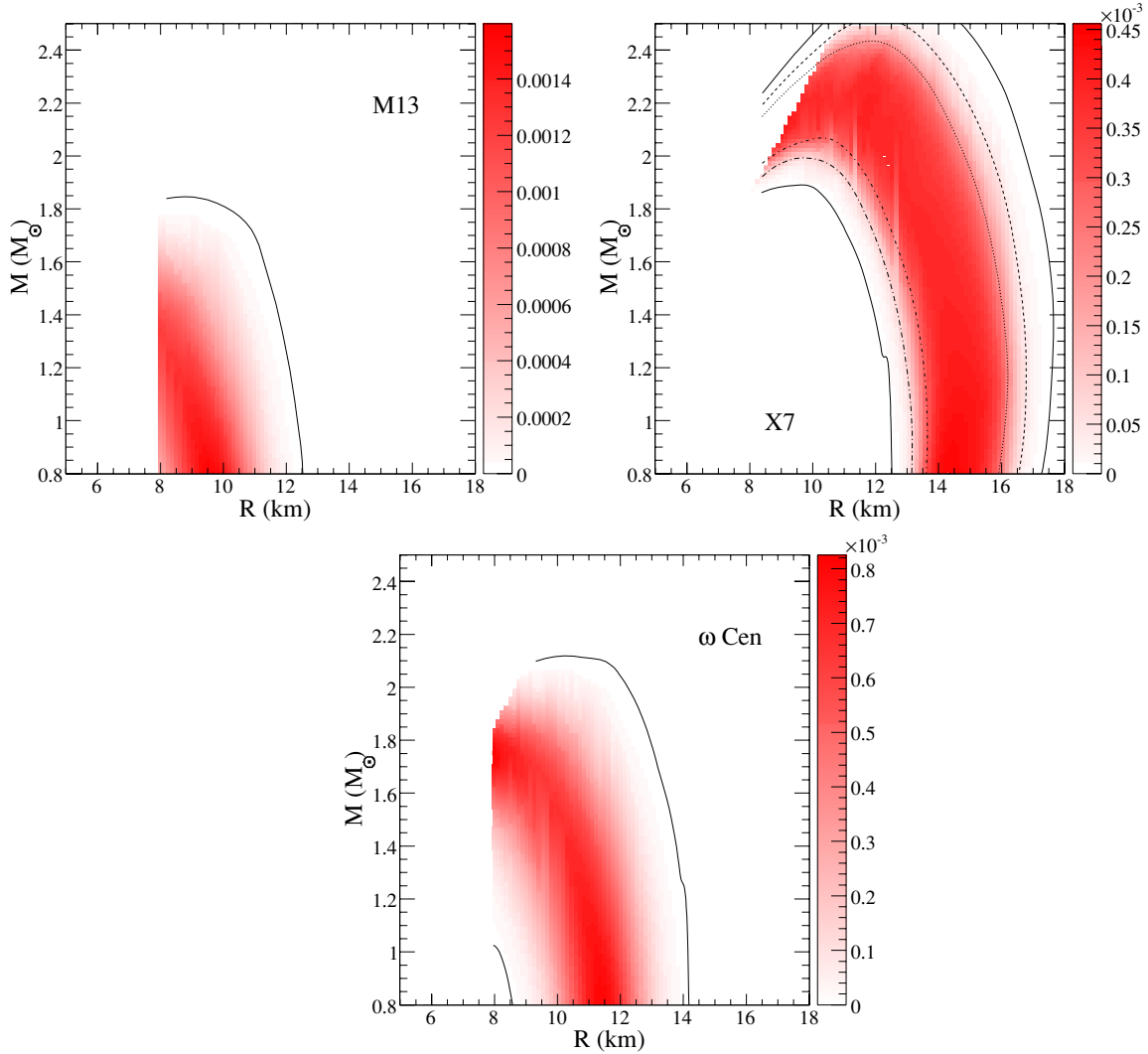


**Figure 4.** Upper left panel: the solid curve is the 99% probability contour in the mass–radius plane for the LMXRB in M13 from Webb & Barret (2007). The red shading shows the probability distribution adopted in this paper. Upper right panel: the various lines are the 68%, 90%, and 99% probability contours for X7 in 47 Tuc from Heinke et al. (2006). The red shading shows the probability distribution adopted in this paper. Lower left panel: the same as the upper left panel except for  $\omega$  Cen. All distributions,  $P_i$ , are normalized so that  $\int P_i dM dR = 1$ .

(A color version of this figure is available in the online journal.)

the data  $D$ ,  $P(D|\mathcal{M})$  is the conditional probability of the data  $D$  given the model  $\mathcal{M}$ , and  $P(\mathcal{M}|D)$  is the conditional probability of the model  $\mathcal{M}$  given the data  $D$ . This latter quantity,  $P(\mathcal{M}|D)$  is what we want to obtain, namely, the probability that a given model is correct given the data.

For many non-overlapping models  $\mathcal{M}_i$  which exhaust the total model space  $\mathcal{M}$ , this relation can be rewritten

$$P(\mathcal{M}_i|D) = \frac{P(D|\mathcal{M}_i)P(\mathcal{M}_i)}{\sum_j P(D|\mathcal{M}_j)P(\mathcal{M}_j)}. \quad (28)$$

For our problem, the model space consists of all of the parameters for the EOS,  $p_{i=1,\dots,N_p}$ , plus values for all of the masses of the neutron stars for which we have data,  $M_{i=1,\dots,N_M}$ . From the parameters,  $p_i$ , we can construct the EOS and solve the TOV equations to get a radius  $R_i$  for each of the neutron star masses  $M_i$ . To be more concise in the following, we refer to our model  $\mathcal{M}(p_1, p_2, \dots, p_{N_p}, M_1, M_2, \dots, M_{N_M})$  as  $\mathcal{M}(p_{1\dots N_p}, M_{1\dots N_M})$ . Applied to this specific problem,

Equation (28) is

$$P[\mathcal{M}(p_{1\dots N_p}, M_{1\dots N_M})|D] = P[D|\mathcal{M}(p_{1\dots N_p}, M_{1\dots N_M})] \times P[\mathcal{M}(p_{1\dots N_p}, M_{1\dots N_M})] \left\{ \int P[D|\mathcal{M}]P[\mathcal{M}]d^N\mathcal{M} \right\}^{-1}, \quad (29)$$

where  $N = N_p + N_M$  is the dimensionality of our model space. The total number of EOS parameters is  $N_p = 8$  and the total number of neutron stars in our data set is  $N_M = 6$ .

We construct our data  $D$  as a set of  $N_M$  probability distributions,  $\mathcal{D}_i(M, R)$  in the  $(M, R)$  plane, which are all normalized to unity, i.e.,

$$\int_{M_{\text{low}}}^{M_{\text{high}}} dM \int_{R_{\text{low}}}^{R_{\text{high}}} dR \mathcal{D}_i(M, R) = 1 \forall i. \quad (30)$$

This normalization ensures that the data set for each neutron star is treated on an equal footing. We choose  $M_{\text{low}} = 0.8 M_\odot$  because current core-collapse supernova simulations fail to

generate lower neutron star masses. The remaining limits,  $M_{\text{high}} = 2.5 M_{\odot}$ ,  $R_{\text{low}} = 5 \text{ km}$ , and  $R_{\text{high}} = 18 \text{ km}$  are extreme enough to ensure that they have no impact on our final results. None of the probability distributions  $\mathcal{D}$  inferred from the data described above have a significant probability for neutron stars outside of these ranges. Note also that the results for the neutron stars in M13 and  $\omega \text{ Cen}$  are cut off in Webb & Barret (2007) for radii below 8 km so our distributions also exhibit the same cutoff.

In order to apply Equation (29) to our problem, we assume that  $P(D|\mathcal{M})$ , the conditional probability of the data given the model, is proportional to the product over the probability distributions  $\mathcal{D}_i$  evaluated at the masses which are chosen in the model and evaluated at the radii which are determined from the model, i.e.,

$$P[D|\mathcal{M}(p_{1\dots N_p}, M_{1\dots N_M})] \propto \prod_{i=1, \dots, N_M} \mathcal{D}_i(M, R)|_{M=M_i, R=R(M_i)}. \quad (31)$$

This implicitly assumes that all of the data distributions  $\mathcal{D}_i$  are independent of each other and also independent of the model assumptions and prior distributions. Another required input for Equation (29) is the prior distribution. We assume that the prior distribution is uniform in all of the  $n_p + n_M$  model parameters, except for a few physical constraints on the parameter space described below. Taking a uniform distribution just means that the  $P(\mathcal{M})$  terms cancel from Equation (29) and the integration limits become the corresponding prior parameter limits.

In the maximum likelihood formalism, the function  $P[D|\mathcal{M}(p_{1\dots N_p}, M_{1\dots N_M})]$  is equivalent to the likelihood function, and maximizing the likelihood function gives the best fit to the data. In the case where the probability distributions represent Gaussian uncertainties, then the best fit is equivalent to a least-squares fit (Bevington & Robinson 2002). In Bayesian inference, model parameters are determined using marginal estimation, where the posterior probability for a model parameter  $p_j$  is given by

$$P[p_j|D](p_j) = \frac{1}{V} \int P[D|\mathcal{M}] dp_1 dp_2 \dots dp_{j-1} dp_{j+1} \dots dp_{N_p} \times dM_1 dM_2 \dots dM_{N_M}, \quad (32)$$

where  $V$  is the denominator in Equation (29), without the model priors that determine the integration limits. The one-dimensional function  $P[p_j|D](p_j)$  represents the probability that the  $j$ th parameter will take a particular value given the observational data. Our problem thus boils down to computing integrals of the form in Equation (32). We use the Metropolis–Hastings algorithm to construct a Markov chain to simulate the distribution  $P[D|\mathcal{M}(p_{1\dots N_p}, M_{1\dots N_M})]$ . For each point, we generate the EOS parameters  $p_i$  and the neutron star masses  $M_i$  from a uniform distribution within limits that are described below. The TOV equations are solved and this generates an  $R(M)$  curve and the radii for each neutron star,  $R_i$ . From these six masses and radii, the weight function  $P[D|\mathcal{M}]$  is computed from Equation (31) and the point is rejected or accepted using the Metropolis algorithm. In order to compute posterior probabilities  $P[p_j|D](p_j)$ , we construct several histograms of the integrand  $P[D|\mathcal{M}]$  from all of the points that were accepted. To construct the  $1\sigma$  regions, we sort the histogram bins by decreasing probability, and select the first  $N$  bins which exhaust 68% of the total weight. A similar procedure is used for the  $2\sigma$  regions. In order to constrain the full EOS of neutron star matter, we histogram the value of the

pressure predicted by each EOS in the Markov chain on a fixed grid of energy density. To create the predicted curve,  $R(M)$ , we construct a histogram of the predicted radii for each EOS in the Markov chain on a fixed mass grid.

This analysis is easily extensible to a different number of EOS parameters or a different number of neutron star data sets. The only issue is that of computer time: the TOV equations must be solved for each point in the model space, and enough points must be selected to cover the model space fully. Another advantage is the explicit presence of the prior distributions,  $P(\mathcal{M})$ . Although we have set these distributions to unity for this work, future work will utilize these terms to examine the impact of constraints on the EOS from terrestrial experiments.

#### 4.2. Parameterization of the EOS

We divide the EOS into four energy density regimes. The region below the transition energy density  $\varepsilon_{\text{trans}} \approx \varepsilon_0/2$  is the crust, for which we use the EOS of Baym et al. (1971) and Negele & Vautherin (1983). Here,  $\varepsilon_0$  is the nuclear saturation energy density; it is convenient to remember that the nuclear saturation baryon density  $0.16 \text{ fm}^{-3}$  corresponds to an energy density of  $\approx 160 \text{ MeV fm}^{-3}$  and a mass density of  $\approx 2.7 \times 10^{14} \text{ g cm}^{-3}$ . For  $\varepsilon_{\text{trans}} < \varepsilon < \varepsilon_1$ , we use a schematic expression representing charge-neutral uniform baryonic matter in beta equilibrium that is compatible with laboratory data. Finally, two polytropic pressure–density relations are used in the regions  $\varepsilon_1 < \varepsilon < \varepsilon_2$  and  $\varepsilon > \varepsilon_2$ . The densities  $\varepsilon_1$  and  $\varepsilon_2$  are themselves parameters of the model. The schematic EOS for  $\varepsilon_{\text{trans}} < \varepsilon < \varepsilon_1$  is taken to be

$$\varepsilon = n_B \left\{ m_B + B + \frac{K}{18}(u-1)^2 + \frac{K'}{162}(u-1)^3 + (1-2x)^2 [S_k u^{2/3} + S_p u^\gamma] + \frac{3}{4} \hbar c x (3\pi^2 n_b x)^{1/3} \right\}, \quad (33)$$

where  $n_B$  is the baryon number density,  $m_B$  is the baryon mass,  $u = n_B/n_0$ , and  $x$  is the proton (electron) fraction. The saturation number density,  $n_0$ , is fixed at  $0.16 \text{ fm}^{-3}$ , the binding energy of saturated nuclear matter,  $B$ , is fixed at  $-16 \text{ MeV}$ , and the kinetic part of the symmetry energy,  $S_k$ , is fixed at  $17 \text{ MeV}$ . The compressibility  $K$ , the skewness  $K'$ , the bulk symmetry energy parameter  $S_v \equiv S_p + S_k$  (where  $S_p$  is the potential part of the symmetry energy), and the density dependence of the symmetry energy  $\gamma$ , are parameters which we constrain to lie within the ranges specified in Table 3. These limits operate as constraints in our otherwise trivial prior distributions,  $P(\mathcal{M})$ . To avoid bias in our results and to ensure that our model space is not overconstrained, we have intentionally made these ranges larger than normally expected from modern models of the EOS of uniform matter which are fit to laboratory nuclei. While in principle the crust EOS for each set of EOS parameters could be different, as described in Steiner (2008), in practice the masses and radii are not strongly affected by changes in the crust at this level. The transition between the crust EOS and the low-density EOS is typically around half of the nuclear saturation density and is determined for each parameter set by ensuring that the energy is minimized as a function of the number density. We have opted, at this stage, not to include correlations between parameters that have been shown to exist from nuclear systematics or neutron matter calculations. For example, the values of  $S_v$  and  $\gamma$  (or, equivalently,  $S_v$  and  $S_s$ , the surface symmetry parameter) are highly correlated (Steiner

**Table 3**  
Prior Limits for the EOS Parameters

Quantity	Lower Limit	Upper Limit
$K$ (MeV)	180	280
$K'$ (MeV)	-1000	-200
$S_v$ (MeV)	28	38
$\gamma$	0.2	1.2
$n_1$ (fm $^{-3}$ )	0.2	1.5
$n_2$ (fm $^{-3}$ )	0.2	2.0
$\varepsilon_1$ (MeV fm $^{-3}$ )	150	600
$\varepsilon_2$ (MeV fm $^{-3}$ )	$\varepsilon_1$	1600

et al. 2005) in liquid drop mass formula fits to nuclear masses. Such correlations will be considered in a future publication.

The last term in Equation (33) is due to electrons. The proton fraction  $x$  is determined as a function of density by the condition of beta equilibrium

$$\frac{\partial \varepsilon}{\partial x} = \hbar c (3\pi^2 n_B x)^{1/3} - 4[S_k u^{2/3} + S_p u^\gamma](1 - 2x) = 0, \quad (34)$$

which has the solution

$$x = \frac{1}{4} [(\sqrt{d+1} + 1)^{1/3} - (\sqrt{d+1} - 1)^{1/3}]^3, \quad (35)$$

where

$$d = \frac{\pi^2 n_B}{288} \left( \frac{\hbar c}{[S_k u^{2/3} + S_p u^\gamma]} \right)^3. \quad (36)$$

We also include muons in our EOS, but they are not included in the above expressions for clarity.

For lack of a clear theoretical understanding of the nature of matter above saturation densities, we parameterize the high-density EOS by a pair of polytropes. Read et al. (2009) have shown that such a parameterization can effectively model a wide variety of theoretical model predictions in this density range. Specifically, for energy densities above a parameterized value  $\varepsilon_1$ , the EOS is

$$P = K_1 \varepsilon^{1+1/n_1}, \quad (37)$$

where  $P$  is the pressure,  $n_1$  is the polytropic index, and  $K_1$  is a coefficient. Note that we are parameterizing the high-density EOS as polytropes in the total energy density  $\varepsilon$  rather than the number density, and that this EOS is assumed to be in beta equilibrium so it automatically includes leptonic contributions. Above a parameterized energy density,  $\varepsilon_2$ , we use a second polytrope

$$P = K_2 \varepsilon^{1+1/n_2}. \quad (38)$$

We choose the transition densities  $\varepsilon_1$  and  $\varepsilon_2$  and the polytropic indices  $n_1$  and  $n_2$  as parameters. The coefficients  $K_1$  and  $K_2$  are determined by pressure and energy density continuity at the transition densities, with values limited such that  $1600 \text{ MeV fm}^{-3} > \varepsilon_2 > \varepsilon_1 > 150 \text{ MeV fm}^{-3}$ . Note that  $1600 \text{ MeV fm}^{-3}$  is either larger than or nearly as large as the central energy density of most configurations. In addition, we limit  $\varepsilon_1 < 600 \text{ MeV fm}^{-3}$ , so that the parameters of the schematic EOS maintain a close connection to their usual definitions in terms of properties near the saturation density. Finally, we limit the polytropic indices with  $0.2 < n_1 < 1.5$  and  $0.2 < n_2 < 2.0$ ; our results are insensitive to this choice of limits.

While phase transitions are included in our models because they will appear like successive polytropes with different indices, some parameter sets do not imply any phase transition,

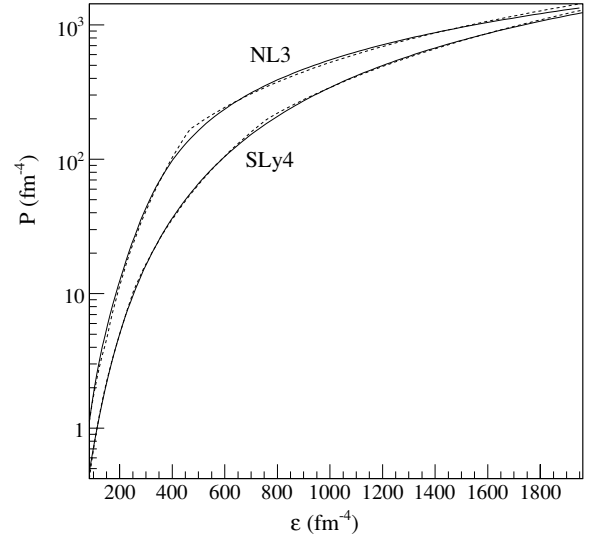


**Figure 5.** Fits of our parameterized EOS (dotted lines) to the Skyrme EOS SLy4 and the field-theoretical EOS NL3 (solid lines).

as they simply model equations of state which have effective polytrope indices which vary with density. Models with more than two strong phase transitions will not be well reproduced by our parameterization, but it is not clear that these models are particularly realistic.

We thus have eight total EOS parameters,  $K$ ,  $K'$ ,  $S_v$ ,  $\gamma$ ,  $n_1$ ,  $n_2$ ,  $\varepsilon_1$ , and  $\varepsilon_2$ , with limiting values summarized in Table 3. In addition to these parameter limits, some combination of parameters must be rejected because they are unphysical. Unphysical combinations include those in which

1. the maximum mass is smaller than  $1.66 M_\odot$ , which is  $2\sigma$  below the mass of PSR J1903+0327,  $1.74 \pm 0.04 M_\odot$  (Champion et al. 2008);
2. the EOS becomes acausal below the central density of the maximum mass star;
3. the EOS is anywhere hydrodynamically unstable, i.e., has a pressure that decreases with increasing density; and
4. the maximum mass star has a maximum stable rotation rate less than 716 Hz, the spin frequency of the fastest known pulsar, Ter 5AD (Hessels et al. 2006). The spin frequency at which equatorial mass shedding commences is given to within a few percent by Haensel et al. (2009):

$$f_K \simeq 1.08 \left( \frac{M}{M_\odot} \right)^{1/2} \left( \frac{10 \text{ km}}{R} \right)^{3/2} \text{ kHz}. \quad (39)$$

There has been claimed possible evidence for a higher spin frequency in XTE J1239–285 (Kaaret et al. 2007), but this observation does not have strong statistical significance and has not been confirmed by subsequent observations.

In addition to these criteria, during the MC generation of neutron star mass sets for the Bayesian analysis, if one of the seven masses is larger than the maximum mass for the selected EOS, that realization is discarded and a new one is selected.

To show that this model accurately represents significantly different EOSs, we fit it to the Skyrme model SLy4 which gives relatively small neutron star radii (of order 10 km for  $M = 1.4 M_\odot$ ), and the field-theoretical model NL3 which gives rather larger radii, of order 15 km, for the same mass. These fits are shown in Figure 5, illustrating that the associated EOSs

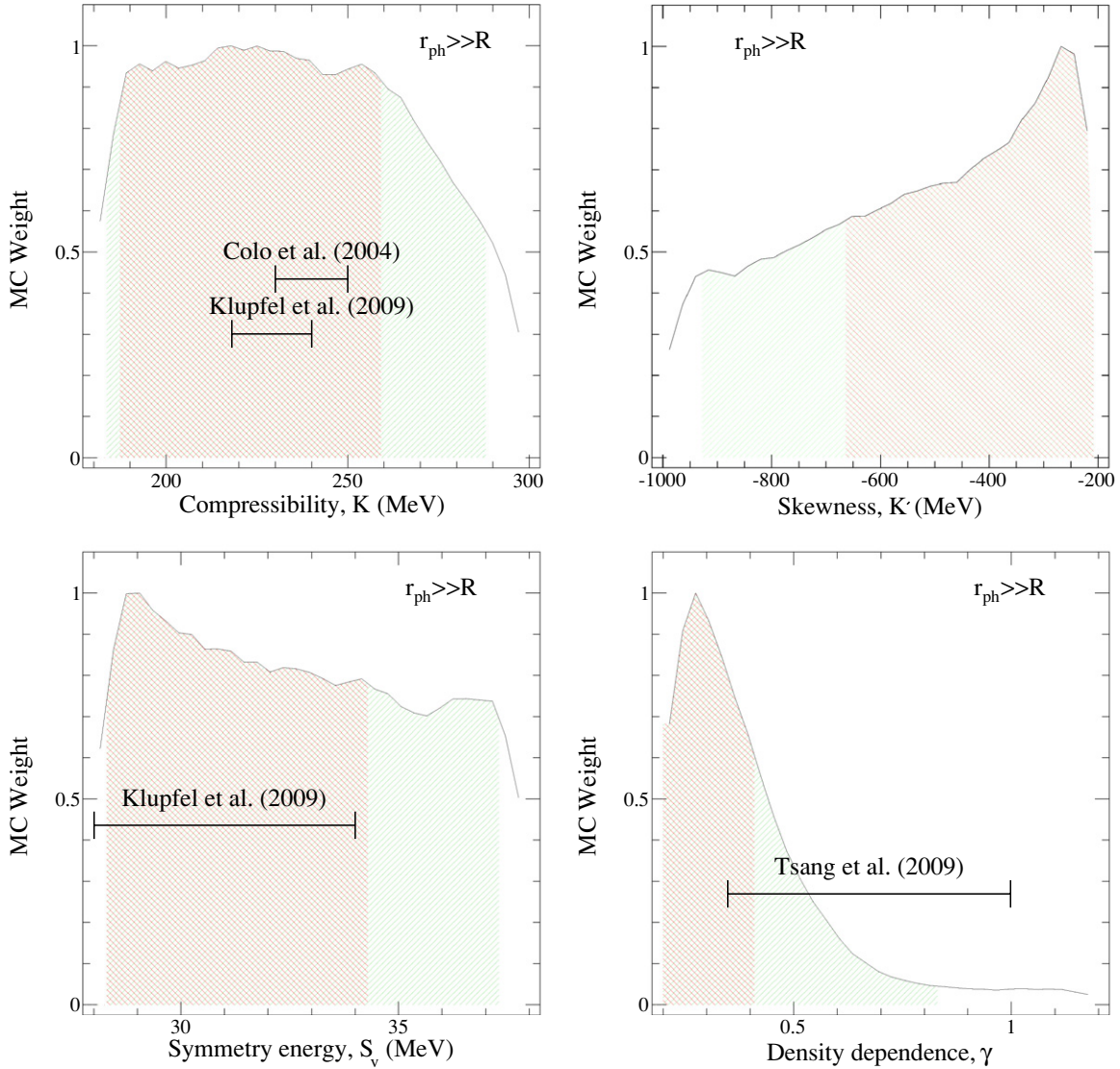


**Figure 6.** Histograms for the compressibility  $K$ , skewness  $K'$ , symmetry energy  $S_v$ , and density dependence of the symmetry energy  $\gamma$ . The  $1\sigma$  (double-hatched) and  $2\sigma$  (single-hatched) confidence regions are also indicated. These results assume  $r_{\text{ph}} \gg R$ . (A color version of this figure is available in the online journal.)

are reproduced to within a few percent. Our parameterization includes many extreme models, including those like NL3 with rather large neutron star radii. We will find below that such models are ruled out, however, by the observational data.

#### 4.3. EOS Results from the Statistical Analysis

We first analyze the EOS implied by observations for the case in which X-ray bursts are modeled assuming  $r_{\text{ph}} \gg R$ . The histograms for the EOS parameters are given in Figures 6–7. The double-hatched (red) and single-hatched (green) regions outline the  $1\sigma$  and  $2\sigma$  confidence regions which are suggested by the simulation. The  $1\sigma$  and  $2\sigma$  parameter limits are summarized in Table 4 along with representative values obtained from terrestrial experiments.

It is remarkable that the inferred ranges for the schematic EOS parameters  $K$ ,  $K'$ ,  $S_v$ , and  $\gamma$  are consistent with the values derived from nuclear experiments. Especially significant is the inferred low value for  $\gamma$ , a parameter which controls the pressure of the EOS in the range of  $1\text{--}3 \varepsilon_0$  and therefore the radii of neutron stars in the mass range  $1 < M/M_\odot < 1.5$  (Lattimer

**Table 4**  
Most Probable Values of the EOS Parameters and their Associated  $1\sigma$  Uncertainties

Quantity	$r_{\text{ph}} \gg R$	$r_{\text{ph}} = R$	Experiment
Schematic EOS parameters			
$K$ (MeV)	$216^{+43}_{-32}$	$190^{+50}_{-7.2}$	230–250 (Colo et al. 2004)
$-K'$ (MeV)	$280^{+410}_{-72}$	$500^{+290}_{-170}$	
$S$ (MeV)	$29^{+5.4}_{-0.9}$	$35^{+2.1}_{-6.3}$	28–34 (Klupfel et al. 2009)
$\gamma$	$0.26^{+0.15}_{-0.06}$	$0.26^{+0.36}_{-0.06}$	0.35–1.0 (Tsang et al. 2009)
High-density EOS parameters			
$n_1$	$0.51^{+0.12}_{-0.16}$	$0.67^{+0.20}_{-0.20}$	
$n_2$	$1.23^{+0.49}_{-0.16}$	$1.23^{+0.59}_{-0.22}$	
$\varepsilon_1$ (MeV fm $^{-3}$ )	$290^{+80}_{-110}$	$320^{+120}_{-93}$	
$\varepsilon_2$ (MeV fm $^{-3}$ )	$620^{+210}_{-170}$	$880^{+430}_{-210}$	

& Prakash 2001). The value of  $\gamma$  also controls the energy and pressure of pure neutron matter. Hebeler & Schwenk (2010) have shown that several recent studies indicate a convergence in



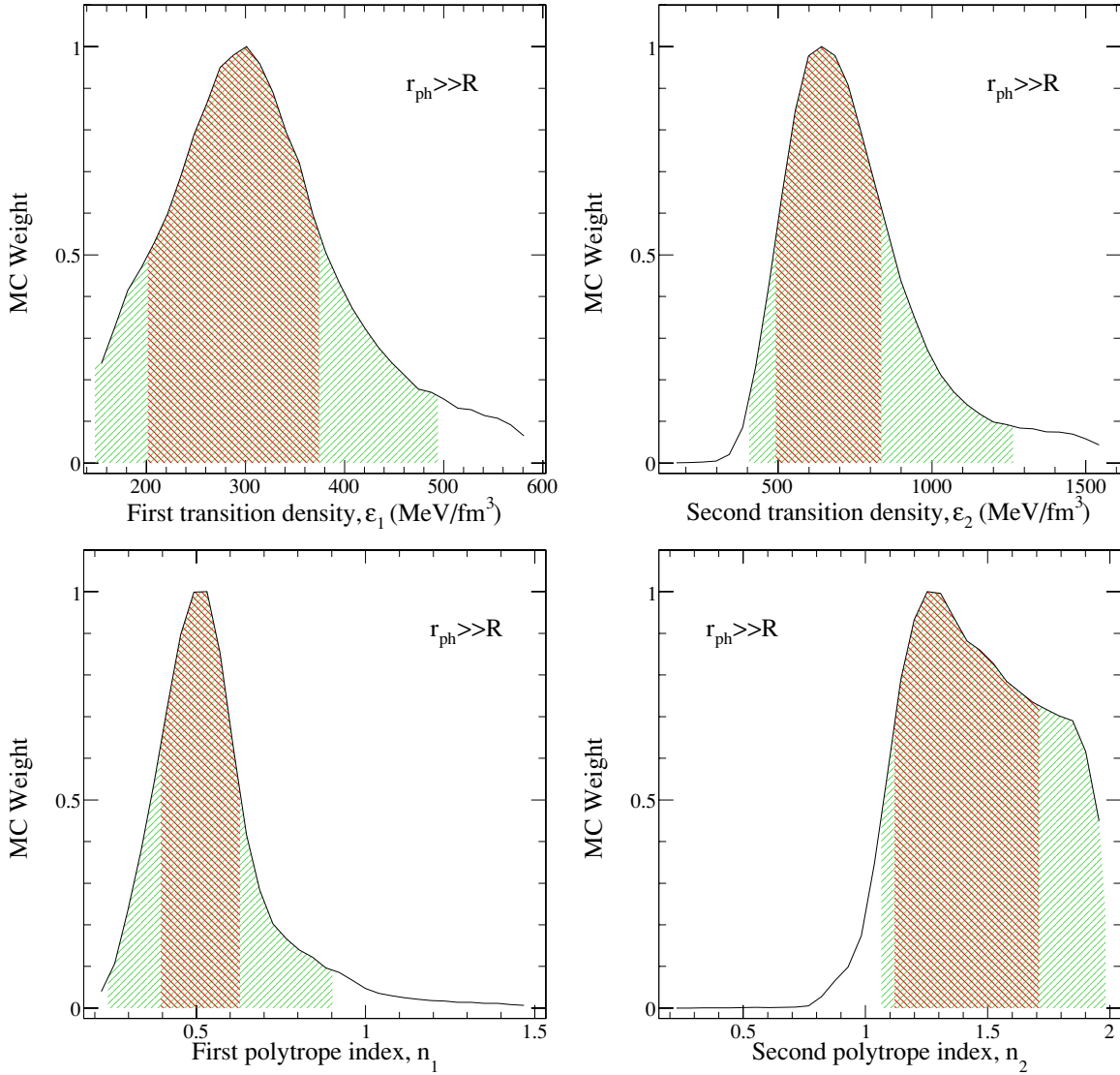


**Figure 7.** Histograms and confidence regions for the transition energy densities,  $\varepsilon_1$  and  $\varepsilon_2$  and the polytropic indices  $n_1$  and  $n_2$ , for  $r_{\text{ph}} \gg R$ . (A color version of this figure is available in the online journal.)

predictions for neutron matter. For the saturation density used there,  $n_0 = 0.16 \text{ fm}^{-3}$ , the mean values of the neutron matter energy and pressure are 16.3 MeV and  $2.5 \text{ MeV fm}^{-3}$ , which imply  $S_v = 32 \text{ MeV}$  and  $\gamma = 0.28$  with the parameterization of Equation (33), well within our predicted ranges.

One must take care in comparing experimental constraints directly to our results, however. The parameters determined experimentally are often “local” quantities, in the sense that they are properties of the EOS only at densities close to saturation. Also, the results from Tsang et al. (2009) mostly constrain the EOS in region near half the saturation density. We have used the schematic EOS parameters over a somewhat larger range of densities, from  $1/2$  to, typically, up to 2 or 3 times the saturation density.

The predicted skewness for the schematic EOS has a relatively small magnitude, centered at  $K' = -280 \text{ MeV}$ . The most probable value for the transition between the schematic EOS and the first polytrope is around twice the saturation density,  $\varepsilon_0$ . The index of the first polytrope is sharply peaked around 0.5, which corresponds to a polytropic exponent  $\gamma_1 = 1 + 1/n_1 \simeq 3$  which is rather large. Coupled with the small magnitude of

the skewness, this implies a quite stiff EOS at supernuclear densities. Finally, note that, typically,  $n_2 > n_1$ , indicating that the EOS softens at high densities. A summary of the results of the EOS parameters for both the schematic EOS and the polytropes is given in Table 4.

We next consider the results of parameter fitting when the X-ray burst data are modeled assuming  $r_{\text{ph}} = R$ . Results are summarized and compared to the previous case in Table 4. Although we do not show histograms for the parameters in this case, their behavior is similar to those of Figures 6 and 7 modulo the different means and variations of the two cases. It is significant that the small value for  $\gamma$  found for the case  $r_{\text{ph}} \gg R$  is duplicated for  $r_{\text{ph}} = R$ , supporting a weak density dependence for the symmetry energy and a consequent small estimate for neutron star radii in the mass range  $1\text{--}1.5 M_\odot$ . We note that Özel et al. (2010) also concluded, on the basis of observations of X-ray bursts, that the implied neutron star radii were relatively small. Özel et al. (2010) obtained radii approximately 1 km smaller than we do, however, for  $r_{\text{ph}} = R$  (which are already 0.5–1 km smaller than those we obtain for  $r_{\text{ph}} \gg R$ ) because their analysis favors the high-redshift solution, and because

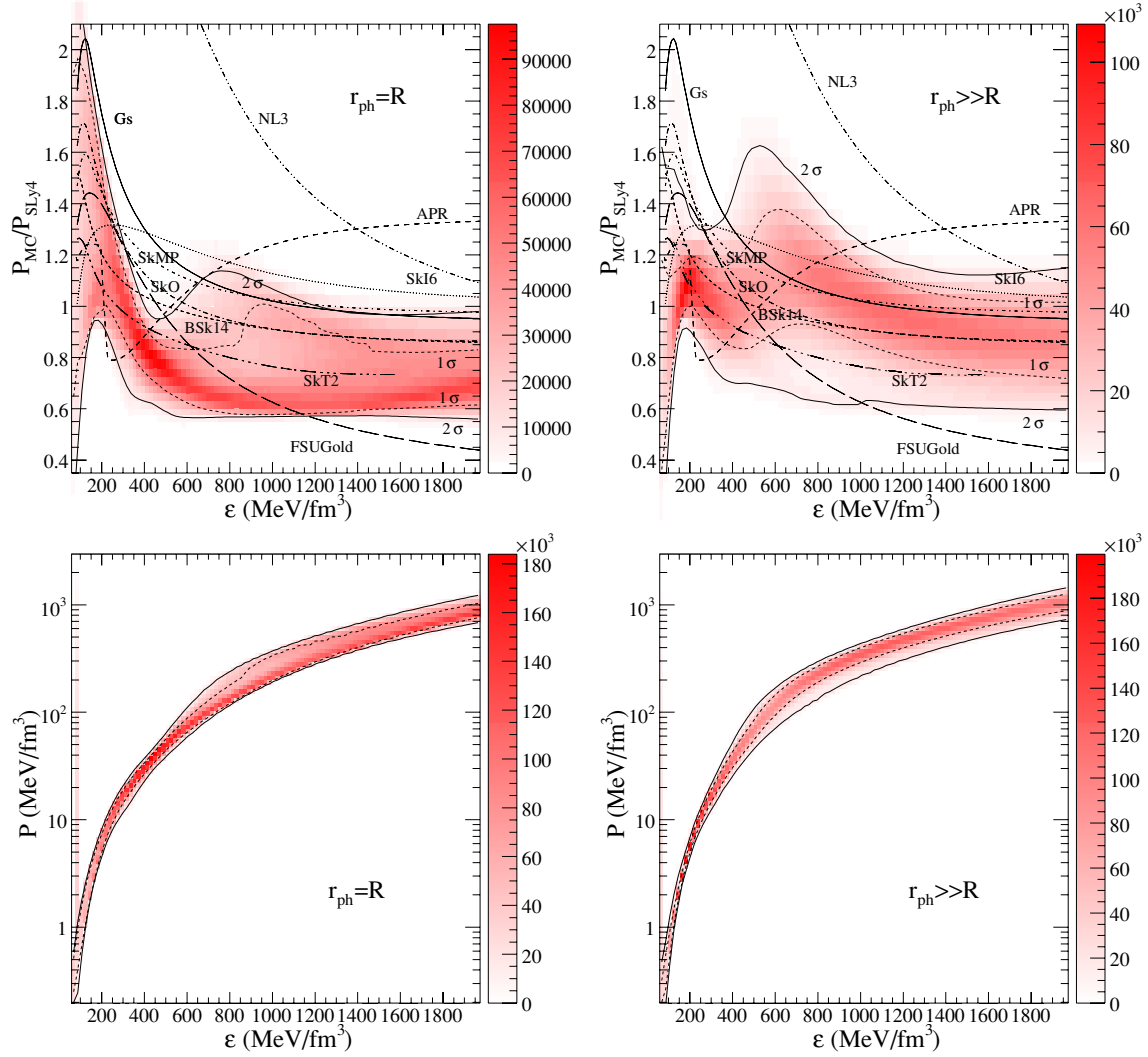


**Figure 8.** Probability distributions from the Bayesian analysis of the parameterized EOS. Upper panels show the ratio of the most probable EOS to the pressure of SLy4. The lower panels show the pressure of the most probable EOS. The left panels show results under the assumption  $r_{\text{ph}} = R$ , and the right panes show results assuming  $r_{\text{ph}} \gg R$ . In all panels, the solid (dotted) contour lines in each panel show the  $2\sigma$  ( $1\sigma$ ) contours implied by the data.

(A color version of this figure is available in the online journal.)

they do not impose the same causality constraint on their MC sampling.

Although the low-density EOS is not strongly affected by the assumption that  $r_{\text{ph}} = R$ , at higher densities this choice leads to a softer EOS: the magnitude of the skewness  $K'$  and first polytropic index  $n_1$  are both larger for the case  $r_{\text{ph}} = R$  (Table 4). The differences between these predicted EOS can be easily seen by referring to Figure 8. Each panel displays an ensemble of one-dimensional histograms over a fixed grid in one of the axes (note that this is not quite the same as a two-dimensional histogram). The bottom panels present the ensemble of histograms of the pressure for each energy density. This was computed in the following way: for each energy density, we determined the histogram bins of pressure which enclose 68% and 95% of the total MC weight. The locations of those regions for each one-dimensional histogram are outlined by dotted and solid lines, respectively, and these form the contour lines. These  $1\sigma$  and  $2\sigma$  contour lines give constraints on the pressure of the EOS as a function of the energy density as implied by the six neutron star data sets and are presented in Tables 5 and 6 along with the most probable EOS for the cases  $r_{\text{ph}} \gg R$  and  $r_{\text{ph}} = R$ ,

respectively. The softer nature of the EOS in the  $r_{\text{ph}} = R$  case is most apparent at the highest energy density, for which the pressure is 10% less than in the  $r_{\text{ph}} \gg R$  case.

The upper panels of Figure 8 display the ensemble of histograms of the ratio of the pressure of the EOS to the pressure of SLy4 over a grid of energy density. The choice of the SLy4 EOS here is essentially arbitrary, and just assists in plotting the results since the pressure varies over a couple orders of a magnitude. The inferred pressure ratio from several Skyrme models is also shown. These Skyrme models were selected in Steiner & Watts (2009) because they are a representative set of the recommended models from Stone et al. (2003) which have symmetry energies which do not become negative at high density. In both the  $r_{\text{ph}} = R$  and  $r_{\text{ph}} \gg R$  cases, there appears to be a softening of the EOS at low densities which is incompatible with some of the Skyrme models. Some models are apparently ruled out independently of assumptions about the radius of the photosphere in X-ray bursts: field-theoretical models like NL3 (Lalazissis et al. 1997), which have stiff symmetry energies; FSUGold (Todd-Rutel & Piekarewicz 2005), which has a softer symmetry energy but becomes

**Table 5**  
Most Probable Values and 68% and 95% Confidence Limits for the Pressure as a Function of Energy Density, for  $r_{\text{ph}} = R$

Energy Density (MeV fm <sup>-3</sup> )	2 $\sigma$ Lower Limit	1 $\sigma$ Lower Limit	Most Probable (MeV fm <sup>-3</sup> )	1 $\sigma$ Upper Limit	2 $\sigma$ Upper Limit
150	1.97	2.02	2.16	3.77	4.11
200	4.57	5.01	5.25	7.37	8.26
250	8.03	9.24	11.99	12.63	13.89
300	11.68	14.23	17.48	18.88	20.76
350	16.23	20.00	22.47	25.95	28.72
400	22.73	26.72	31.96	33.82	37.29
450	30.51	34.73	40.75	43.69	48.43
500	38.28	43.97	49.72	56.10	63.79
550	47.44	53.93	61.06	71.02	84.56
600	58.92	65.10	72.64	87.99	110.8
650	70.68	77.15	82.31	107.2	139.4
700	84.24	90.40	97.50	128.9	172.2
750	99.90	105.2	117.6	153.4	207.4
800	115.6	121.0	132.3	179.6	239.2
850	132.5	136.5	155.8	206.1	270.3
900	151.0	155.8	173.8	263.0	304.9
950	169.7	177.5	191.6	302.2	338.5
1000	190.8	197.9	207.7	337.3	371.1
1050	213.2	220.1	236.5	364.2	406.2
1100	234.8	243.0	253.5	389.8	439.3
1140	257.2	268.1	277.5	423.2	476.7
1200	280.2	294.5	308.3	459.7	516.3
1250	300.5	321.1	343.4	462.8	551.2
1300	323.4	346.2	379.2	504.2	585.8
1350	352.0	369.9	411.0	528.2	622.8
1400	381.2	398.4	436.4	561.5	666.9
1450	402.4	432.6	453.1	612.5	712.3
1500	427.1	460.4	502.1	643.9	749.2
1550	459.3	484.6	518.8	676.0	799.6
1600	480.0	520.7	550.8	718.2	848.6

too soft at high density; and the Akmal, Pandharipande, and Ravenhall EOS (APR; Akmal et al. 1998), which becomes too stiff at high densities. The nearly vertical nature of APR for energy densities just over 200 MeV fm<sup>-3</sup> is due to the phase transition in APR to matter which includes a  $\pi^0$  condensate. Even after applying a Gibbs phase construction, the pressure increases only very slowly with density in the small mixed phase region.

#### 4.4. Mass and Radius Results from the Statistical Analysis

The upper panels in Figure 9 present our results for the predicted mass–radius relation according to our two assumptions regarding the photospheric radius for X-ray bursts. They give the ensemble of histograms of the radius over a fixed grid in neutron star mass. The width of the contours at masses below 1  $M_{\odot}$  tends to be large because the available neutron star mass and radius data generally imply larger masses. In general, the implied  $M$ – $R$  curve suggests relatively small radii, which is consistent with our conclusions regarding the softness of the nuclear symmetry energy in the vicinity of the nuclear saturation density. Tables 7 and 8 summarize the 1 $\sigma$  and 2 $\sigma$  contour lines from these panels, and give as well the most probable  $M$ – $R$  curve. The assumption that  $r_{\text{ph}} = R$  implies smaller radii for neutron star masses greater than about 1.3  $M_{\odot}$  and perhaps very small radii for masses in excess of 1.5  $M_{\odot}$ . This is suggestive of the onset of a phase transition above the nuclear saturation density or perhaps simply the approach to the neutron star maximum mass limit in this case. The mass and radius contour lines, determined in the same way as for Figure 8, are also given in the figure, and summarized in Tables 7 and 8. The radii in the  $r_{\text{ph}} = R$

case average about 1 km less than in the  $r_{\text{ph}} \gg R$  case, except around 1.4  $M_{\odot}$ , where the difference is about 0.4 km.

The lower panels in Figure 9 summarize the output probability distributions for  $M$  and  $R$  for the six neutron stars which were used in this analysis. Note that the scales have been modified, and these output probability distributions are much smaller than the input distributions given in Figures 1, 2, and 4. The combination of several neutron star mass and radius measurements with the assumption that all neutron stars must lie on the same mass–radius curve puts a significant constraint on the mass and radius of each object. Note that these output probability distributions closely match the implied  $M$  versus  $R$  curves presented in the upper panels of Figure 9. The tendency for smaller radii when  $M > 1.3$ –1.4  $M_{\odot}$  is apparent.

The  $M$  and  $R$  constraints for each object are given in Table 9, with their corresponding 1 $\sigma$  uncertainties. The three PRE burst sources suggest masses near 1.5  $M_{\odot}$  and the radii near 11 km in the case where  $r_{\text{ph}} = R$ . We have already observed that this agreement is due to the extreme restrictions placed on the acceptability of points during the MC sampling. In the case  $r_{\text{ph}} \gg R$ , the PRE burst sources are predicted to have a wider range of masses, from 1.3 to 1.6 solar masses. The quiescent LMXB masses tend to be smaller, but are strongly dependent on assumptions about the radius of the photosphere in the PRE burst sources. Particularly uncertain is the mass for X7. The observations imply a rather large value of  $R_{\infty}$ , which is compatible with a small radius if the mass is large ( $r_{\text{ph}} \gg R$ ), or a large radius if the mass is small ( $r_{\text{ph}} = R$ ). The stars in M13 and  $\omega$  Cen show the opposite trend. They have small values of  $R_{\infty}$  which is compatible with small radii in the  $r_{\text{ph}} \gg R$  case

**Table 6**Most Probable Values and 68% and 95% Confidence Limits for the Pressure as a Function of Energy Density, for  $r_{\text{ph}} \gg R$ 

Energy Density (MeV fm <sup>-3</sup> )	2 $\sigma$ Lower Limit	1 $\sigma$ Lower Limit	Most Probable (MeV fm <sup>-3</sup> )	1 $\sigma$ Upper Limit	2 $\sigma$ Upper Limit
150	1.84	2.00	2.15	2.52	3.25
200	4.44	4.97	5.76	6.06	6.88
250	8.10	9.14	10.67	11.50	12.71
300	12.34	14.61	15.87	19.08	21.43
350	18.19	21.52	24.43	29.16	34.17
400	25.32	30.46	35.80	42.86	52.07
450	34.56	41.54	49.11	60.99	77.97
500	45.32	55.19	69.75	84.54	107.7
550	57.47	73.14	89.83	114.1	138.1
600	70.62	94.02	115.5	145.0	168.1
650	85.07	116.8	149.7	175.8	199.8
700	100.8	141.0	173.2	206.8	230.6
750	115.7	165.8	203.3	237.8	263.8
800	131.5	190.6	232.7	268.8	297.7
850	154.0	214.9	254.1	299.9	330.9
900	175.0	239.7	277.4	331.6	364.7
950	196.7	264.4	310.0	364.2	399.7
1000	217.0	289.9	336.2	397.8	437.6
1050	236.5	316.5	371.9	432.7	474.1
1100	260.3	343.5	414.4	468.9	509.8
1140	282.1	369.6	458.2	504.7	547.6
1200	307.3	395.4	457.7	541.2	592.7
1250	333.2	424.7	494.3	581.2	639.6
1300	356.8	454.5	550.4	622.4	680.9
1350	381.4	481.1	603.9	660.6	726.2
1400	407.7	512.5	608.5	704.7	777.2
1450	434.2	542.8	672.0	749.1	824.9
1500	460.5	572.1	661.5	791.8	877.5
1550	487.5	606.4	732.5	840.2	932.8
1600	514.9	635.2	734.9	884.5	979.8

**Table 7**Most Probable Values and 68% and 95% Confidence Limits for Neutron Star Radii of Fixed Mass, for  $r_{\text{ph}} = R$ 

Mass ( $M_{\odot}$ )	2 $\sigma$ Lower Limit	1 $\sigma$ Lower Limit	Most Probable (km)	1 $\sigma$ Upper Limit	2 $\sigma$ Upper Limit
1.0	11.06	11.35	12.09	12.62	13.31
1.1	10.97	11.28	11.87	12.35	13.00
1.2	10.90	11.23	11.69	12.11	12.65
1.3	10.81	11.13	11.42	11.85	12.28
1.4	10.68	10.98	11.32	11.60	11.93
1.5	10.42	10.75	11.04	11.37	11.65
1.6	9.93	10.37	10.87	11.17	11.47
1.7	9.44	10.05	10.65	11.12	11.42
1.8	9.60	10.14	10.65	11.06	11.38

**Table 8**Most Probable Values and 68% and 95% Confidence Limits for Neutron Star Radii of Fixed Mass, for  $r_{\text{ph}} \gg R$ 

Mass ( $M_{\odot}$ )	2 $\sigma$ Lower Limit	1 $\sigma$ Lower Limit	Most Probable (km)	1 $\sigma$ Upper Limit	2 $\sigma$ Upper Limit
1.0	11.29	11.75	12.09	12.30	12.57
1.1	11.31	11.71	11.94	12.28	12.51
1.2	11.30	11.65	11.96	12.24	12.47
1.3	11.24	11.58	11.81	12.21	12.45
1.4	11.13	11.49	11.83	12.18	12.45
1.5	10.94	11.39	11.83	12.17	12.45
1.6	10.63	11.30	11.70	12.17	12.49
1.7	10.42	11.21	11.70	12.13	12.54
1.8	10.43	11.10	11.57	12.05	12.47



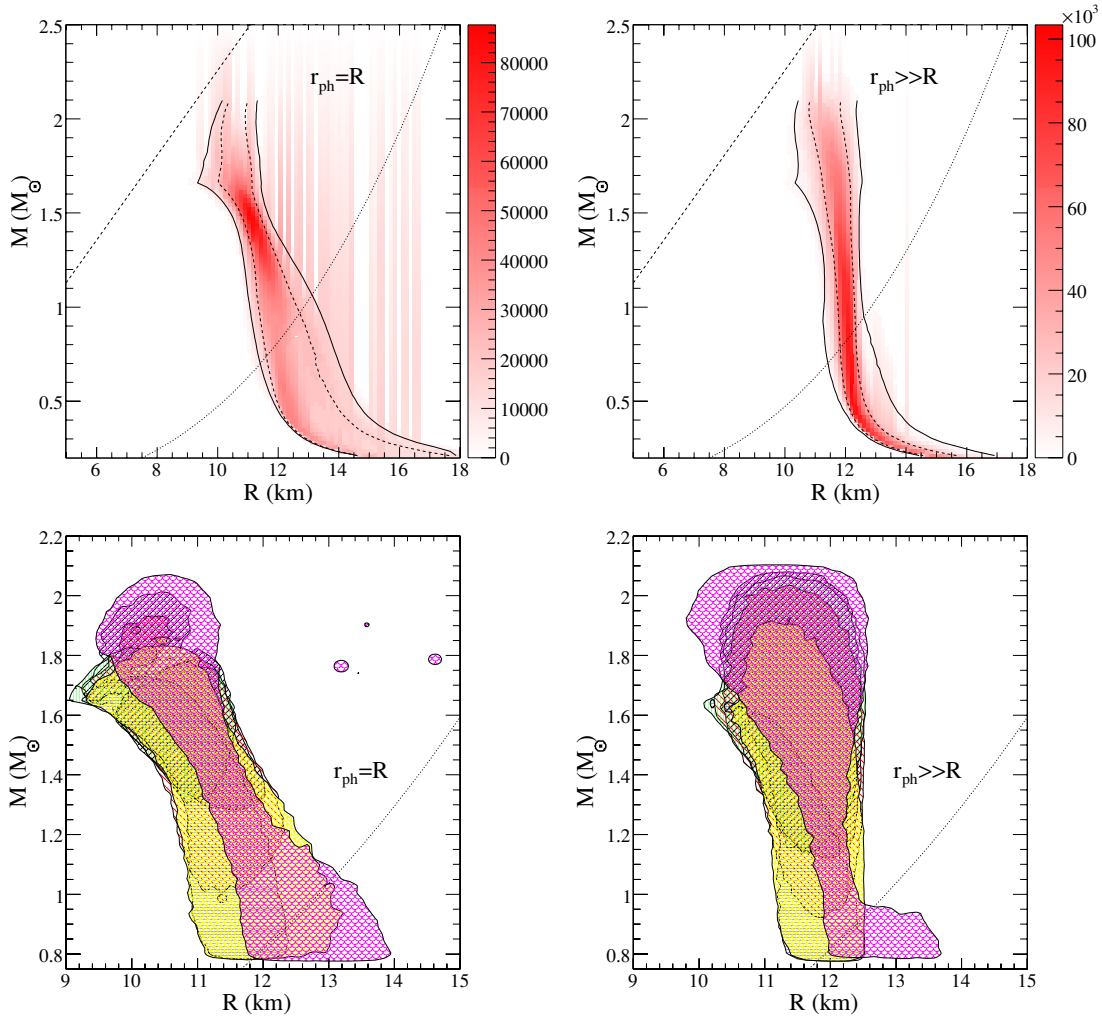


**Figure 9.** Upper panels give the probability distributions for the mass vs. radius curves implied by the data, and the solid (dotted) contour lines show the  $2\sigma$  ( $1\sigma$ ) contours implied by the data. The lower panes summarize the  $2\sigma$  probability distributions for the six objects considered in the analysis. The left panels show results under the assumption  $r_{\text{ph}} = R$ , and the right panes show results assuming  $r_{\text{ph}} \gg R$ . The dashed line in the upper left is the limit from causality. The dotted curve in the lower right of each panel represents the mass-shedding limit for neutron stars rotating at 716 Hz.

(A color version of this figure is available in the online journal.)

**Table 9**

Most Probable Values for Masses and Radii for Neutron Stars Constrained to Lie on One Mass Versus Radius Curve

Object	$r_{\text{ph}} = R$		$r_{\text{ph}} \gg R$	
	$M (M_{\odot})$	$R \text{ (km)}$	$M (M_{\odot})$	$R \text{ (km)}$
4U 1608–522	$1.52^{+0.22}_{-0.18}$	$11.04^{+0.53}_{-1.50}$	$1.64^{+0.34}_{-0.41}$	$11.82^{+0.42}_{-0.89}$
EXO 1745–248	$1.55^{+0.12}_{-0.36}$	$10.91^{+0.86}_{-0.65}$	$1.34^{+0.450}_{-0.28}$	$11.82^{+0.47}_{-0.72}$
4U 1820–30	$1.57^{+0.13}_{-0.15}$	$10.91^{+0.39}_{-0.92}$	$1.57^{+0.37}_{-0.31}$	$11.82^{+0.42}_{-0.82}$
M13	$1.48^{+0.21}_{-0.64}$	$11.04^{+1.00}_{-1.28}$	$0.901^{+0.28}_{-0.12}$	$12.21^{+0.18}_{-0.62}$
$\omega$ Cen	$1.43^{+0.26}_{-0.61}$	$11.18^{+1.14}_{-1.27}$	$0.994^{+0.51}_{-0.21}$	$12.09^{+0.27}_{-0.66}$
X7	$0.832^{+1.19}_{-0.051}$	$13.25^{+1.37}_{-3.50}$	$1.98^{+0.10}_{-0.36}$	$11.3^{+0.95}_{-1.03}$

if the mass is relatively small. In general, the predicted radii of all stars range from about 10 km to 12.5 km, with the exception of X7 which may have a large radius. Note that a 13 km radius for an  $0.8 M_{\odot}$  star is beyond the limit implied by rotation at 716 Hz and thus if the neutron star in X7 is observed to spin rapidly enough, a much larger mass and smaller radius would be implied instead.

The largest difference between the predicted equations of state between the  $r_{\text{ph}} = R$  and  $r_{\text{ph}} \gg R$  cases is the high-

density behavior. This leads to large differences in the predicted maximum masses. The probability distributions for the maximum neutron star mass are given in Figure 10, along with the associated  $1\sigma$  confidence regions. The two probability distributions are arbitrarily normalized so that their peak is unity. These results are strongly dependent on assumptions of the photospheric radius at touchdown. The two-peaked behavior in the case  $r_{\text{ph}} = R$  suggests a possible phase transition could match the data and implies a maximum mass very close to the observed limit of  $1.66 M_{\odot}$ . This result is similar to that claimed by Özel et al. (2010), but there it is stated that the results are incompatible with a nucleonic EOS. Our results do not support this extreme interpretation. Although the neutron star radii implied by this analysis are small, they are not small enough to require a phase transition; for neutron stars of mass  $1.4 M_{\odot}$ , radii smaller than 10 km can be generated by purely nucleonic equations of state (Steiner et al. 2005).

## 5. DISCUSSION

In this paper, we have determined an empirical dense matter EOS from a heterogeneous data set containing PRE bursts and quiescent thermal emission from X-ray transients. Previous

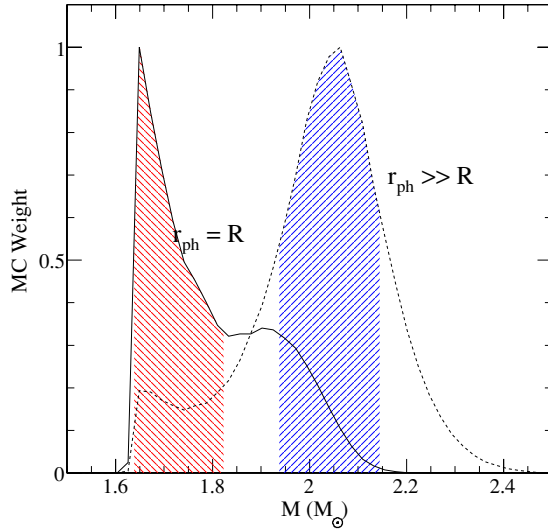


**Figure 10.** Probability distributions for the maximum mass. Because of the observation of a neutron star of at least  $1.66 M_{\odot}$ , we reject all curves for which  $M_{\max} < 1.66 M_{\odot}$  and thus the probability is cut off below this value. The shaded regions indicate the  $1\sigma$  confidence regions.

(A color version of this figure is available in the online journal.)

works (Özel 2006; Özel et al. 2009; Güver et al. 2010a, 2010b) have demonstrated the potential utility of PRE bursts for determining neutron star masses and radii. Their analysis assumes that the photosphere at touchdown has fully retreated to the quiescent radius, and that the high-redshift solution is favored. We argue that their model requires reexamination. First, we find no grounds on which the high-redshift solution in the case  $r_{\text{ph}} = R$  could be favored. Second, internal consistency (i.e., the obligatory rejection of an overwhelming number of MC realizations) implies the assumption that  $r_{\text{ph}} = R$  is suspect and should be generalized. We then explored an alternative, that the radius of the photosphere is extended and does not recede until later in the observed burst. A larger photosphere indeed provides internal consistency without requiring strong cuts on the observed values for flux, normalization, distance, and composition.

There are other sources of systematic errors in the PRE burst model. Bouloukos et al. (2010) found that *RXTE*/PCA spectra of bursts from 4U 1820–30 were better fit by Planck or Bose–Einstein spectra rather than Comptonized spectra with large color-correction factors. If the color-correction factor is indeed of order unity, then the high color temperatures would indicate a locally super-Eddington flux, even in the tail of the burst (Ebisuzaki et al. 1984). In addition, at near-Eddington fluxes there are other possible complications, such as a photon bubble instability (Hsu et al. 1997) that may impact the observed properties of a PRE X-ray burst.

A recent analysis of PRE bursts in 4U 1724–307 by Suleimanov et al. (2010) also found that the photosphere is somewhat extended at touchdown,  $r_{\text{ph}} \approx 2R$ . Using a new model of the atmosphere (the details of which are not yet published), they obtain masses and radii that are both larger than we would have found. This result is principally due to a larger value of the color-correction factor,  $f_c$ , predicted by their model atmosphere. It is 10%–15% larger than what one would obtain from the model of Madej et al. (2004) for the same values of  $F/F_{\text{Edd}}$ , surface gravity  $g$ , and composition. In this case, we find values of  $\alpha \propto f_c^{-2}$  which are about 25% larger and  $R_{\infty} \propto f_c^2$  that are about 25% smaller than Suleimanov et al. (2010) did. Assuming

$r_{\text{ph}} \gg R$ , the predicted mass scales with  $f_c^2$ . When we analyze 4U 1724–307 with the lower value of  $f_c$ , we get masses and radii that are consistent with those from the other three PRE burst sources. This highlights an important avenue for future work, namely, that a clearer understanding of the atmosphere and, in particular,  $f_c$  are essential.

Further progress in using PRE bursts to constrain neutron star masses and radii clearly requires better models of the spectral evolution during X-ray bursts. It is important to note that increases in the precision of mass and radius estimates are not absolutely necessary, as we have shown that existing errors, large as they are, do not inhibit placing interesting limits to the EOS when combined with other observations. It is very important, however, to resolve the uncertainty regarding the location of the photospheric radius at “touchdown” and to characterize systematic uncertainties, including potential correlations between  $F_{\text{TD}}$ ,  $A$ ,  $f_c$ , and  $X$  in the spectral models. Also, should a larger range in  $f_c$  be required, then the uncertainties on masses and radii will increase accordingly.

Our results imply that the EOS in the vicinity of the nuclear saturation density is relatively soft. As shown by Lattimer & Prakash (2001), this is primarily due to the weak dependence of the nuclear symmetry energy with density. This conclusion is robust with respect to variations in how PRE burst sources are modeled, and is strengthened by the small values of  $R_{\infty}$  deduced for the globular cluster LMXB sources in M13 and  $\omega$  Cen. This conclusion has immediate and important ramifications for laboratory nuclear physics, in particular for the scheduled parity-violating electron scattering measurement of the neutron skin thickness of  $^{208}\text{Pb}$  (Michaels et al. 2000; Horowitz et al. 2001). In the context of the liquid droplet model, the ratio of the surface and volume symmetry coefficients can be expressed as (Steiner et al. 2005)

$$\frac{S_s}{S_v} = \frac{9E_{s0}}{K} \frac{I_2}{I_1}, \quad (40)$$

where  $E_{s0} \simeq 19$  MeV is the surface energy coefficient for symmetric nuclei. The integrals  $I_1$  and  $I_2$  for the schematic EOS described by Equation (33) are given by

$$\begin{aligned} I_1 &= \int_0^1 \sqrt{u(1-u)} \sqrt{1-a(1-u)} du, \\ I_2 &= \int_0^1 \sqrt{u} \left[ \frac{S_v}{S_k u^{2/3} + (S_v - S_k) u^\gamma} - 1 \right] \\ &\quad \times \frac{1}{1-u} \frac{1}{\sqrt{1-a(1-u)}} du, \end{aligned} \quad (41)$$

where  $a = K'/(9K)$ . The predicted neutron excess in the center of a nucleus ( $N, Z$ ) is then

$$\delta = \frac{N-Z}{N+Z} \left( 1 + \frac{S_s}{S_v A^{1/3}} \right)^{-1}, \quad (42)$$

and the neutron skin thickness is

$$\delta R = \sqrt{\frac{3}{5}} \frac{2r_0}{3} \frac{S_s}{S_v} \frac{\delta}{1-\delta^2}, \quad (43)$$

where  $r_0 = (4\pi n_0/3)^{-1/3}$ . With a value of  $\gamma = 0.26$  and  $a = -0.141$  and errors as established in Table 4, we deduce  $S_s/S_v \simeq 1.5 \pm 0.3$  and  $\delta R(^{208}\text{Pb}) \simeq 0.15 \pm 0.02$  fm, a value at the lower end of expectations.

We also conclude that in our preferred model, in which the photospheric radius is not restricted to be the stellar radius, the EOS at high densities is stiff enough to support a maximum mass of order  $2 M_{\odot}$  or greater. This result is supported by the simultaneous observations of LMXB sources with both small and large values of  $R_{\infty}$ , if one rejects the possibility of the existence of neutron stars with masses less than about  $1 M_{\odot}$ . The latter condition seems to be borne out by models of massive star supernovae, which strongly suggest that protoneutron stars are born with high trapped lepton fractions and moderate entropies. Hydrostatic stability requires, in this case, that protoneutron stars are bound only if their mass exceeds about  $1 M_{\odot}$  (Strobel et al. 1999), ruling out the existence of cold, catalyzed neutron stars of smaller masses. Had this assumption been used as a prior condition in our analysis, the LMXB sources with small values of  $R_{\infty}$  would further support solutions with EOS parameters favoring large maximum masses.

Obviously, more neutron star observations with mass and radius constraints would enable one to improve our constraints. It is a particular advantage of our methodology that new observations can be integrated into the formalism easily, if estimates of a two-dimensional probability distribution of mass and radius can be made. As pointed out by Heinke et al. (2006), it is particularly important that atmosphere models treat the surface gravity self-consistently. In particular, spectral features would be very constraining, and although the most recent result from Cottam et al. (2002) has not been verified in longer observations (Cottam et al. 2008), future determinations of the surface gravity may provide strong constraints. Ho & Heinke (2009) also demonstrated that constraints on the mass and radius of the Cas A supernova remnant may be obtained. These constraints are roughly consistent with our  $r_{\text{ph}} \gg R$  results described above.

Although we did not include the estimate of the mass and radius ( $M = 1.7 \pm 0.3 M_{\odot}$  and  $R = 11.5 \pm 1.2 \text{ km}$ ) of RX J1856–3754 (Pons et al. 2002; Walter et al. 2010) in our baseline fit, we found them to be remarkably consistent with those of the other six neutron stars. All of the results we obtained for the parameters of the EOS, the pressure versus energy density curve, the mass versus radius curve, our estimate of the maximum mass, and the predicted individual masses and radii for all six other sources were unchanged to within  $1\sigma$ . For example, the most probable radius of a  $1.4 M_{\odot}$  star would change by less than 0.01 km and the most probable pressure at an energy density of  $1000 \text{ MeV fm}^{-3}$  would increase by 0.03%.

In addition to X-ray bursts, quiescent LMXBs, and thermally emitting isolated neutron stars, other potential methods for determining neutron star masses and radii exist. These include neutron star seismology (Samuelsson & Andersson 2007; Steiner & Watts 2009), pulse profiles in X-ray pulsars (Leahy et al. 2009; Morsink & Leahy 2009), and moment of inertia measurements in relativistic binaries (Lattimer & Schutz 2005). Gravitational wave signals of neutron star mergers may also provide significant constraints (Ferrari et al. 2010). Measurements of the thickness of the neutron star crust, which controls the crust cooling of transiently accreting LMXBs (Shternin et al. 2007; Brown & Cumming 2009) as well as the distribution of observed cooling curves compared to a minimal cooling model (e.g., Page et al. 2009), could also constrain neutron star masses and radii.

The Bayesian analysis in Section 4 is a novel procedure for combining mass and radius constraints from disparate objects to form new constraints on the mass versus radius curve and

the EOS of dense matter. The construction of the EOS from astrophysical observations has also been recently addressed in Read et al. (2009), Özel & Psaltis (2009), and Özel et al. (2010). Read et al. (2009) showed that piecewise polytropes with relatively few parameters could effectively describe more sophisticated models for a high-density EOS, but confined attention to constraints stemming from observations limiting the neutron star maximum mass and maximum spin rate. They did not attempt reconstruction of the EOS from simultaneous mass and radius measurements. We therefore obtain stronger constraints on the EOS, but have utilized observational data which contain significant systematic uncertainties. Özel & Psaltis (2009) examined the constraints on the EOS obtained from a synthetic data set obtained with simultaneous mass and radius measurements of either 5% or 10% accuracy for three separate objects; they found that although individual EOS parameters were difficult to estimate precisely, significant correlations between them could be obtained. The Jacobian technique employed in Özel & Psaltis (2009) is a simple approximation of our full Markov Chain MC method. That Jacobian technique requires that the number of EOS parameters and the number of neutron stars are equal, and thus provides only an incomplete marginalization over the EOS parameters.

One could imagine various alternatives to the statistical procedure in Section 4. One possibility is the use of prior distributions to represent either astrophysical or nuclear input. Neutron star masses in some double-pulsar systems are well measured, and could provide a prior mass distribution. It is not clear, however, that either LMXBs or isolated neutron stars follow this same initial mass function. As mentioned above, there are strong theoretical reasons to suspect that neutron stars cannot be formed with less than about  $1.0 M_{\odot}$ . In the analysis above, we chose  $0.8 M_{\odot}$  to ensure that the boundary does not interfere with results near the protoneutron star minimum mass. There are several nuclear physics observables which can be used to constrain the EOS through measurements of properties like the compressibility and the symmetry energy. Several authors have also computed the EOS of neutron matter directly from nucleon–nucleon interactions (Tolos et al. 2008; Hebeler & Schwenk 2010), and we have found that our predicted EOS is consistent with these studies. In the context of this work, information from calculations of the neutron matter EOS, neutron skin thicknesses, the surface symmetry–volume symmetry energy correlation observed from mass formula fits (Steiner et al. 2005), information from giant dipole resonances, and so forth, could also provide constraints for the schematic EOS parameters described above. We have chosen not to use this information in this work, in part to ensure that our results are free from extra model dependences. Future work on implementing more nuclear physics input into the analysis of the observational data is certainly warranted.

One might also question, for the high-density EOS, whether or not our prior distributions for the polytropic indices ought to be treated as uniform, as a uniform distribution in the polytropic index is different than, for example, a uniform distribution in the pressure at any fixed energy density, or in the polytropic exponent. Finally, one could consider reformulating the model directly in terms of the observables like flux and distance instead of the “two-step” procedure we have used above which uses an MC simulation to generate masses and radii from the observables for each neutron star, and then afterward performs a Bayesian analysis from the output of these initial MC results. This alternative would strongly disfavor

$r_{\text{ph}} = R$ , since so many MC realizations must be rejected in this picture.

It is important to note that the constraints we have obtained are a guide, but will likely require revision in the future. Because we only used six mass and radius measurements a single additional measurement could have a significant impact on our results. Alternatively, if one of the six input probability distributions used above changes significantly because, for example, of a new understanding of systematic uncertainties, our final constraints on the EOS would change accordingly. We have already noted that there is significant tension on our results from assumptions about the photospheric radius of X-ray bursts, and also from the fact that the neutron star in M13 has a small value of  $R_\infty$  while X7 in Terzan 5 has a much larger value of  $R_\infty$ .

It is possible that there exist extreme models which live in very small regions of parameter space and are not fully sampled in this work. One example of such an EOS would be those which exhibit the “twinning” phenomenon, i.e., the presence of a turning point in the mass versus radius curve which admits a new family of compact neutron stars (Glendenning & Kettner 2000; Schaffner-Bielich et al. 2002). Such solutions should be addressed in future work.

Özel et al. (2010) claim that constraints from the PRE burst sources imply that equations of state which contain only nucleonic degrees of freedom are inconsistent with data. We disagree with their conclusion. Although we find that the EOS must be quite soft at moderate densities, we do find many nucleonic models which are consistent with the data. More importantly, however, we find that the conclusion of extreme softening evaporates if we use a slightly different model for the PRE burst sources that accounts for systematic uncertainties. The inclusion of mass and radius data from other neutron star sources supports our interpretation of the PRE burst sources. While our results do not rule out a phase transition at supernuclear densities, extreme softening of the EOS is not compatible with observations. Rather, the implication is that the maximum mass is likely large, greater than  $1.8 M_\odot$ .

We thank D. Galloway, A. Kundu, J. Linnemann, M. Prakash, S. Reddy, and R. Rutledge for useful discussions and critical comments on this manuscript. A.W.S. and E.F.B. are supported by the Joint Institute for Nuclear Astrophysics at MSU under NSF PHY grant 08-22648 and by NASA ATP grant NNX08AG76G. J.M.L. acknowledges research support from the U.S. DOE grant DE-AC02-87ER40317. The TOV solver, benchmark EOSs, fitting and data analysis routines were obtained from the O2scl library found at <http://o2scl.sourceforge.net>. A.W.S., E.F.B., and J.M.L. acknowledge the kind hospitality of the ECT\*, where this paper was started. E.F.B. and J.M.L. also thank the Yukawa Institute for Theoretical Physics for a providing a stimulating environment where this work received extensive discussion among the participants.

## APPENDIX

### OBSERVATIONS OF TYPE-I X-RAY BURSTS

In this appendix, we describe in detail our probability distributions for the angular emitting area, or normalization, the distance, the touchdown flux, and the photospheric hydrogen mass fraction for the three sources with PRE bursts used in this analysis. We also note, where appropriate, how the distances compare to the value obtained by assuming the maximum flux

is less than the Eddington value,

$$D < \left( \frac{GMc}{\kappa F_{\text{max},\infty}} \right) = 17.1 \text{ kpc} \left[ \left( \frac{M}{1.4 M_\odot} \right) \times \left( \frac{10^{-8} \text{ erg cm}^{-2} \text{ s}^{-1}}{F_{\text{max},\infty}} \right) \right]^{1/2}. \quad (\text{A1})$$

#### A.1. EXO 1745–248

*Normalization.* The normalization factors obtained from the two PRE bursts in Özel et al. (2009) are  $A/(1 \text{ km}^2 \text{ kpc}^{-2}) = 1.04 \pm 0.01$  and  $1.30 \pm 0.01$ . These two measurements differ significantly, and this means that either the color-correction factors for the two bursts differ by roughly 6% or the geometry of the two bursts is different. It is not clear how to resolve this conflict. Özel et al. (2009) use a boxcar distribution with  $A = 1.16 \text{ km}^2 \text{ kpc}^{-2}$  and  $\Delta A = 0.13 \text{ km}^2 \text{ kpc}^{-2}$ , which represents the choice with the minimum possible uncertainty. We instead choose a Gaussian centered at  $A = 1.17 \text{ km}^2 \text{ kpc}^{-2}$  with  $\sigma_A = 0.13 \text{ km}^2 \text{ kpc}^{-2}$ , which ensures that the two observations are included to within  $1\sigma$ . This choice is consistent with the objects below, which also have normalization factors which are simulated with Gaussian distributions, but with notably smaller uncertainties.

*Distance.* EXO 1745–248 is located in the globular cluster Terzan 5. Ortolani et al. (2007) analyzed the distance to Terzan 5 using both the NICMOS instrumental magnitudes and the calibrations from Stephens et al. (2000) and Cohn et al. (2002). The combined distance estimation is  $D = 5.9 \pm 0.9 \text{ kpc}$ , where the uncertainty has been obtained from the standard deviation of the three different distance measurements, suggesting a Gaussian with the same standard deviation. On the basis that the distance measurement from the NICMOS instrumental magnitudes was independent of photometric calibrations and thus more accurate, Özel et al. (2009) used the NICMOS distance of  $D = 6.3 \text{ kpc}$  with  $\Delta D = 0.32 \text{ kpc}$ . This choice assigns, however, a zero probability to a distance of 5.9 kpc, the central value suggested in Ortolani et al. (2007). Until this distance measurement is more clearly determined, we choose a Gaussian distribution with  $D = 6.3 \text{ kpc}$  and  $\sigma_D = 0.6 \text{ kpc}$ .

*Touchdown flux.* We employ the result from Özel et al. (2009), which is a Gaussian distribution with  $F_{\text{TD},\infty} = 6.25 \text{ erg cm}^{-2} \text{ s}^{-2}$  and  $\sigma_F = 0.2 \text{ erg cm}^{-2} \text{ s}^{-2}$ .

*Hydrogen mass fraction.* Galloway et al. (2008) noted that EXO 1745–248 has exhibited long Type-I bursts with estimated values of  $\int dt F_{\text{persistent}} / \int dt F_{\text{burst}} \approx GM/R/E_{\text{nuc}} \approx 20\text{--}46$ . These long bursts do not always show a strong thermal evolution (D. K. Galloway 2009, private communication); but if they are indeed thermonuclear in origin, then the low ratio of persistent to burst fluence indicates H-rich fuel and larger values of  $X$ . In contrast to the determination of  $X$  from these long bursts, this object has also been identified as an ultracompact binary in Heinke et al. (2003), through a phenomenological assessment of its spectral properties, suggesting that  $X$  is small,  $0 < X < 0.1$ . The radius expansion bursts have short durations, which would be consistent for ignition of a pure He layer (i.e., the hydrogen is consumed by the stable hot CNO cycle). We retain the full range of hydrogen composition,  $0 < X < 0.7$ .

#### A.2. 4U 1608–522

*Normalization.* The normalization factors for the four PRE bursts are  $A/(1 \text{ km}^2 \text{ kpc}^{-2}) = 3.267 \pm 0.047$ ,  $3.302 \pm 0.049$ ,



$3.258 \pm 0.054$ , and  $3.170 \pm 0.047$  (Güver et al. 2010a). We use the average from Güver et al. (2010a),  $3.246 \pm 0.024$ .

*Distance.* Güver et al. (2010a) give a Gaussian distribution with  $D = 5.8$  kpc and  $\sigma_D = 2.0$  kpc with a cutoff below 3.9 kpc. We also employ this result. We note that if the flux is indeed less than the Eddington value, then  $D < 4.36 \text{ kpc} (M/1.4 M_\odot)^{1/2}$  for the central value of the touchdown flux.

*Touchdown flux.* Two of the four PRE bursts gave a value for the touchdown flux,  $F_{\text{TD},\infty} = (15.58 \pm 0.82) \text{ erg cm}^{-2} \text{ s}^{-2}$  and  $(15.14 \pm 1.05) \text{ erg cm}^{-2} \text{ s}^{-2}$  (Güver et al. 2010a). The value  $(15.41 \pm 0.65) \text{ erg cm}^{-2} \text{ s}^{-2}$  was obtained from the fit in Güver et al. (2010a).

*Hydrogen mass fraction.* The bursts in 4U 1608–522 suggest an accretion rate in of 3%–5%  $\dot{M}_{\text{Edd}}$ , which suggests H ignition (Galloway et al. 2008); the brighter bursts from this system are of short duration, however, so it is likely that much of the hydrogen is consumed via the HCNO cycle prior to He ignition. As with EXO 1745–248, we use the full range  $0 < X < 0.7$ .

### A.3. 4U 1820–30

*Normalization.* The three PRE bursts for which a normalization was obtained give  $A/(1 \text{ km}^2 \text{ kpc}^{-2}) = 0.8886 \pm 0.0373$ ,  $0.9668 \pm 0.0339$ , and  $0.9040 \pm 0.0200$  (Güver et al. 2010b). We use the value quoted in Güver et al. (2010b),  $0.9198 \pm 0.0186$ .

*Distance.* 4U 1820–30 is in the globular cluster NGC 6624. Güver et al. (2010b) use a boxcar distribution from 6.8 kpc to 9.6 kpc, to reflect two distance measurements of  $(7.6 \pm 0.4) \text{ kpc}$  (Kuulkers et al. 2003) and  $(8.4 \pm 0.6) \text{ kpc}$  (Valenti et al. 2007). We employ a Gaussian distribution centered at 8.2 kpc with  $\sigma_D = 0.7 \text{ kpc}$  since the 95% confidence regions for this Gaussian is the same as the range suggested by the boxcar in Güver et al. (2010b). A more recent determination (Dotter et al. 2010) gives an apparent distance of 10.2 kpc, which when corrected for extinction gives 8.1 kpc, consistent with our value described above.

*Touchdown flux.* Five of the bursts have a measured touchdown flux:  $F_{\text{TD},\infty}/(10^{-8} \text{ erg cm}^{-2} \text{ s}^{-2}) = 5.33 \pm 0.27$ ,  $5.65 \pm 0.20$ ,  $5.12 \pm 0.15$ ,  $5.24 \pm 0.19$ , and  $5.42 \pm 0.16$  (Güver et al. 2010b). The fit in Güver et al. (2010b) gives  $(5.31 \pm 0.10) \times 10^{-8} \text{ erg cm}^{-2} \text{ s}^{-2}$ , which we use here.

*Hydrogen mass fraction.* This object is likely an ultracompact binary with an H-poor donor (King & Watson 1986; Stella et al. 1987). Although evolutionary models do not exclude the possibility that the envelope could contain some H ( $X \lesssim 0.1$ ; Podsiadlowski et al. 2002), a comparison of burst properties with theoretical ignition models suggests H-poor fuel (Cumming 2003). We fix  $X = 0$  for this source.

## REFERENCES

- Akmal, A., Pandharipande, V. R., & Ravenhall, D. G. 1998, *Phys. Rev. C*, **58**, 1804
- Baym, G., Pethick, C., & Sutherland, P. 1971, *ApJ*, **170**, 299
- Bevington, P., & Robinson, D. K. 2002, *Data Reduction and Error Analysis for the Physical Sciences* (New York: McGraw-Hill)
- Bildsten, L., Salpeter, E. E., & Wasserman, I. 1992, *ApJ*, **384**, 143
- Boutloukos, S., Miller, M. C., & Lamb, F. K. 2010, *ApJ*, **721**, 15
- Brown, E. F., Bildsten, L., & Rutledge, R. E. 1998, *ApJ*, **504**, L95
- Brown, E. F., & Cumming, A. 2009, *ApJ*, **698**, 1020
- Burwitz, V., Haberl, F., Neuhauser, R., Predehl, P., Trümper, J., & Zavlin, V. E. 2003, *A&A*, **399**, 1109
- Burwitz, V., Zavlin, V. E., Neuhauser, R., Predehl, P., & Trümper Brinkman, A. C. 2001, *A&A*, **379**, L35
- Champion, D. J., et al. 2008, *Science*, **320**, 1309
- Cohn, H. N., Lugger, P. M., Grindlay, J. E., & Edmonds, P. D. 2002, *ApJ*, **571**, 818
- Colo, G., Van Giai, N., Meyer, J., Bennaceur, K., & Bonche, P. 2004, *Phys. Rev. C*, **70**, 024307
- Cottam, J., Paerels, F., & Mendez, M. 2002, *Nature*, **420**, 51
- Cottam, J., Paerels, F., Méndez, M., Boirin, L., Lewin, W. H. G., Kuulkers, E., & Miller, J. M. 2008, *ApJ*, **672**, 504
- Cumming, A. 2003, *ApJ*, **595**, 1077
- Damen, E., Magnier, E., Lewin, W. H. G., Tan, J., Penninx, W., & van Paradijs, J. 1990, *A&A*, **237**, 103
- Dotter, A., et al. 2010, *ApJ*, **708**, 698
- Ebisuzaki, T., Hanawa, T., & Sugimoto, D. 1983, *PASJ*, **35**, 17
- Ebisuzaki, T., & Nakamura, N. 1988, *ApJ*, **328**, 251
- Ebisuzaki, T., Sugimoto, D., & Hanawa, T. 1984, *PASJ*, **36**, 551
- Ferrari, V., Gualtieri, L., & Pannarale, F. 2010, *Phys. Rev. D*, **81**, 064026
- Galloway, D. K., Munro, M. P., Hartman, J. M., Psaltis, D., & Chakrabarty, D. 2008, *ApJS*, **179**, 360
- Galloway, D. K., Özel, F., & Psaltis, D. 2008, *MNRAS*, **387**, 268
- Glendenning, N. K. 1992, *Phys. Rev. D*, **46**, 4161
- Glendenning, N. K., & Kettner, C. 2000, *A&A*, **353**, L9
- Grinstead, C. M., & Snell, J. L. 1997, *Introduction to Probability* (Providence, RI: American Mathematical Society)
- Güver, T., Özel, F., Cabrera-Lavers, A., & Wroblewski, P. 2010a, *ApJ*, **712**, 964
- Güver, T., Wroblewski, P., Camarota, L., & Özel, F. 2010b, *ApJ*, **719**, 1807
- Haensel, P., & Zdunik, J. L. 1990, *A&A*, **227**, 431
- Haensel, P., Zdunik, J. L., Bejger, M., & Lattimer, J. M. 2009, *A&A*, **502**, 605
- Hebel, K., & Schwenk, A. 2010, *Phys. Rev. C*, **82**, 014314
- Heinke, C. O., Edmonds, P. D., Grindlay, J. E., Lloyd, D. A., Cohn, H. N., & Lugger, P. M. 2003, *ApJ*, **590**, 809
- Heinke, C. O., Rybicki, G. B., Narayan, R., & Gridlay, J. E. 2006, *ApJ*, **644**, 1090
- Hessels, J. W. T., Ransom, S. M., Stairs, I. H., Freire, P. C. C., Kaspi, V. M., & Camilo, F. 2006, *Science*, **311**, 1901
- Ho, W. C. G., & Heinke, C. O. 2009, *Nature*, **462**, 71
- Ho, W. C. G., Kaplan, D. L., Chang, P., van Adelsberg, M., & Potekhin, A. Y. 2007, *MNRAS*, **375**, 821
- Hoffman, J. A., Lewin, W. H. G., Doty, J., Jernigan, J. G., Haney, M., & Richardson, J. A. 1978, *ApJ*, **221**, L57
- Horowitz, C. J., Pollock, S. J., Souder, P. A., & Michaels, R. 2001, *Phys. Rev. C*, **63**, 025501
- Hsu, J. J. L., Arons, J., & Klein, R. I. 1997, *ApJ*, **478**, 663
- in't Zand, J. J. M., & Weinberg, N. N. 2010, arXiv:1001.0900
- Kaaret, P., et al. 2007, *ApJ*, **657**, L97
- King, A. R., & Watson, M. G. 1986, *Nature*, **323**, 105
- Klupfel, P., Reinhard, P., Burvenich, T. J., & Maruhn, J. A. 2009, *Phys. Rev. C*, **79**, 034310
- Kuulkers, E., den Hartog, P. R., in't Zand, J. J. M., Verbunt, F. W. M., Harris, W. E., & Cocchi, M. 2003, *A&A*, **399**, 663
- Lalazissis, G. A., König, J., & Ring, P. 1997, *Phys. Rev. C*, **55**, 540
- Lattimer, J. M., & Prakash, M. 2001, *ApJ*, **550**, 426
- Lattimer, J. M., & Prakash, M. 2005, *Phys. Rev. Lett.*, **94**, 111101
- Lattimer, J. M., & Prakash, M. 2007, *Phys. Rep.*, **442**, 109
- Lattimer, J. M., & Schutz, B. F. 2005, *ApJ*, **629**, 979
- Leahy, D. A., Morsink, S. M., Chung, Y., & Chou, Y. 2009, *ApJ*, **691**, 1235
- London, R. A., Taam, R. E., & Howard, W. M. 1986, *ApJ*, **306**, 170
- Madej, J., Joss, P. C., & Rozanska, A. 2004, *ApJ*, **602**, 904
- Michaels, R., Souder, P. A., & Urciuoli, G. M. 2000, *Jefferson Laboratory Proposal*, PR-00-003
- Morsink, S. M., & Leahy, D. A. 2009, arXiv:0911.0887
- Negele, J. W., & Vautherin, D. 1983, *Nucl. Phys. A*, **207**, 298
- Oppenheimer, J. R., & Volkoff, G. M. 1939, *Phys. Rev.*, **55**, 374
- Ortolani, S., Barbuy, B., Bica, E., Zoccali, M., & Renzini, A. 2007, *A&A*, **470**, 1043
- Özel, F. 2006, *Nature*, **441**, 1115
- Özel, F., Baym, G., & Guver, T. 2010, arXiv:1002.3153
- Özel, F., Güver, T., & Psaltis, D. 2009, *ApJ*, **693**, 1775
- Özel, F., & Psaltis, D. 2009, *Phys. Rev. D*, **80**, 103003
- Paczynski, B. 1983, *ApJ*, **267**, 315
- Paczynski, B., & Anderson, N. 1986, *ApJ*, **302**, 1
- Page, D., Lattimer, J. M., Prakash, M., & Steiner, A. W. 2009, *ApJ*, **707**, 1131
- Podsiadlowski, P., Rappaport, S., & Pfahl, E. D. 2002, *ApJ*, **565**, 1107
- Pons, J. A., Walter, F. M., Lattimer, J. M., Prakash, M., Neuhauser, R., & An, P. 2002, *ApJ*, **564**, 981
- Read, J. S., Lackey, B. D., Owen, B. J., & Friedman, J. L. 2009, *Phys. Rev. D*, **79**, 124032
- Rutledge, R. E., Bildsten, L., Brown, E. F., Pavlov, G. G., & Zavlin, V. E. 1999, *ApJ*, **514**, 945

- Samuelsson, L., & Andersson, N. 2007, *MNRAS*, **374**, 256
- Schaffner-Bielich, J., Hanauske, M., Stöcker, H., & Greiner, W. 2002, *Phys. Rev. Lett.*, **89**, 171101
- Shternin, P. S., Yakovlev, D. G., Haensel, P., & Potekhin, A. Y. 2007, *MNRAS*, **382**, L43
- Steiner, A. W. 2008, *Phys. Rev. C*, **77**, 035805
- Steiner, A. W., Prakash, M., Lattimer, J. M., & Ellis, P. J. 2005, *Phys. Rep.*, **411**, 325
- Steiner, A. W., & Watts, A. L. 2009, *Phys. Rev. Lett.*, **103**, 181101
- Stella, L., White, N. E., & Priedhorsky, W. 1987, *ApJ*, **315**, L49
- Stephens, A. W., Frogel, J. A., Ortolani, S., Davies, R., Jablonka, P., Renzini, A., & Michael, R. R. 2000, *AJ*, **119**, 419
- Stone, J. R., Miller, J. C., Koncewicz, R., Stevenson, P. D., & Strayer, M. R. 2003, *Phys. Rev. C*, **68**, 034324
- Strobel, K., Schaab, C., & Weigel, M. K. 1999, *A&A*, **350**, 497
- Strohmayer, T. E., & Bildsten, L. 2004, in *Compact Stellar X-ray Sources*, ed. W. Lewin & M. van der Klis (Cambridge: Cambridge Univ. Press), 113
- Suleimanov, V., Poutanen, J., Revnivtsev, M., & Werner, K. 2010, *arXiv:1004.4871*
- Tiengo, A., & Mereghetti, S. 2007, *ApJ*, **657**, L101
- Todd-Rutel, B. G., & Piekarewicz, J. 2005, *Phys. Rev. Lett.*, **95**, 122501
- Tolman, R. C. 1939, *Phys. Rev.*, **55**, 364
- Tolos, L., Friman, B., & Schwenk, A. 2008, *Nucl. Phys.*, **A806**, 105
- Tsang, M. B., Zhang, Y., Danielewicz, P., Famiano, M., Li, Z., Lynch, W. G., & Steiner, A. W. 2009, *Phys. Rev. Lett.*, **102**, 122701
- Valenti, E., Ferraro, F. R., & Origlia, L. 2007, *AJ*, **133**, 1287
- van Kerkwijk, M. H., & Kaplan, D. L. 2007, *Ap&SS*, **308**, 191
- van Kerkwijk, M. H., & Kaplan, D. L. 2008, *ApJ*, **673**, L163
- van Kerkwijk, M. H., & Kulkarni, S. R. 2001, *A&A*, **380**, 221
- van Paradijs, J. 1979, *ApJ*, **234**, 609
- van Paradijs, J. 1982, *A&A*, **107**, 51
- van Paradijs, J., Dotani, T., Tanaka, Y., & Tsuru, T. 1990, *PASJ*, **42**, 633
- Walter, F., & Lattimer, J. M. 2002, *ApJ*, **576**, L145
- Walter, F. M., Eisenbeiss, T., Lattimer, J. M., Kim, B., Hambaryan, V., & Neuhäuser, R. 2010, *arXiv:1008.1709*
- Walter, F. M., Wolk, S. J., & Neuhäuser, R. 1996, *Nature*, **379**, 233
- Webb, N. A., & Barret, D. 2007, *ApJ*, **671**, 727
- Weinberg, N. N., Bildsten, L., & Schatz, H. 2005, *ApJ*, **639**, 1018
- Woosley, S. E., et al. 2004, *ApJS*, **151**, 75
- Zavlin, V. E., Pavlov, G. G., & Shibanov, Y. A. 1996, *A&A*, **315**, 141